AGU PUBLICATIONS

JGR

Journal of Geophysical Research: Space Physics

RESEARCH ARTICLE
10.1002/2016JA022499

Special Section:
Energetic Electron Loss and its Impacts on the Atmosphere

Key Points:
- Heliospheric plasmasheet impingements on the magnetosphere lead to relativistic electron losses
- Compressing the magnetosphere causes generation of coherent EMIC waves which confine electron losses to small region of dayside ionosphere
- Energy deposition and ionization at low altitudes may cause Wilcox effect and Tinsley effect

Correspondence to:
B. T. Tsurutani,
bruce.t.tsurutani@jpl.nasa.gov

Citation:
Tsurutani, B. T., et al. (2016), Heliospheric plasma sheet (HPS) impingement onto the magnetosphere as a cause of relativistic electron dropouts (REDs) via coherent EMIC wave scattering with possible consequences for climate change mechanisms, *J. Geophys. Res. Space Physics*, *121*, doi:10.1002/2016JA022499.

Received 6 FEB 2016
Accepted 25 AUG 2016
Accepted article online 31 AUG 2016

Heliospheric plasma sheet (HPS) impingement onto the magnetosphere as a cause of relativistic electron dropouts (REDs) via coherent EMIC wave scattering with possible consequences for climate change mechanisms

B. T. Tsurutani[1], R. Hajra[2], T. Tanimori[3], A. Takada[3], R. Bhanu[4], A. J. Mannucci[1], G. S. Lakhina[5], J. U. Kozyra[6,7], K. Shiokawa[8], L. C. Lee[4], E. Echer[2], R. V. Reddy[4], and W. D. Gonzalez[2]

[1]Jet Propulsion Laboratory, California Institute of Technology, Pasadena, California, USA, [2]Instituto Nacional de Pesquisas Espacias, Sao Jose dos Campos, Brazil, [3]Faculty of Science, Kyoto University, Kyoto, Japan, [4]Academia Sinica, Taipei, Taiwan, [5]Indian Institute of Geomagnetism, Navi Mumbai, India, [6]Department of Space Physics, University of Michigan, Ann Arbor, Michigan, USA, [7]National Science Foundation, Washington, District of Columbia, USA, [8]Institute for Space Earth Environmental Research, Nagoya University, Nagoya, Japan

Abstract A new scenario is presented for the cause of magnetospheric relativistic electron decreases (REDs) and potential effects in the atmosphere and on climate. High-density solar wind heliospheric plasmasheet (HPS) events impinge onto the magnetosphere, compressing it along with remnant noon-sector outer-zone magnetospheric ~10-100 keV protons. The betatron accelerated protons generate coherent electromagnetic ion cyclotron (EMIC) waves through a temperature anisotropy ($T_{\perp}/T_{||} > 1$) instability. The waves in turn interact with relativistic electrons and cause the rapid loss of these particles to a small region of the atmosphere. A peak total energy deposition of ~3×10^{20} ergs is derived for the precipitating electrons. Maximum energy deposition and creation of electron-ion pairs at 30-50 km and at < 30 km altitude are quantified. We focus the readers' attention on the relevance of this present work to two climate change mechanisms. Wilcox et al. (1973) noted a correlation between solar wind heliospheric current sheet (HCS) crossings and high atmospheric vorticity centers at 300 mb altitude. Tinsley et al. (1994) has constructed a global circuit model which depends on particle precipitation into the atmosphere. Other possible scenarios potentially affecting weather/climate change are also discussed.

1. Introduction

The presence of relativistic electrons in the Earth's outer magnetosphere has been well-established since the late 1950s [*Van Allen and Frank*, 1959; *Vernov et al.*, 1960; *O'Brien et al.*, 1962; *Frank et al.*, 1963; *Freeman*, 1964; *Paulikas and Blake*, 1979; *Baker et al.*, 1994; *Friedel et al.*, 2002]. Present thinking is that these electrons are accelerated to ~ MeV energies by the interaction of ~100 keV electrons with electromagnetic whistler-mode waves called chorus [*Horne and Thorne*, 1998; *Miyoshi et al.*, 2003; *Meredith et al.*, 2003a; *Omura et al.*, 2008; *Reeves et al.*, 2013; *Thorne et al.*, 2013; *Boyd et al.*, 2014]. Where do the ~100 keV electrons and the chorus come from? The overall picture is quite complex. One starts with interplanetary Alfvén waves in high-speed solar wind streams (HSSs) [*Belcher and Davis*, 1971]. The southward component of these Alfvén waves lead to magnetic reconnection at the dayside magnetopause [*Tsurutani et al.*, 1990, 1995]. Midnight sector magnetic reconnection in the magnetotail leads to plasmasheet injections into the nightside magnetosphere with the adiabatic compression of the injected electrons and protons to energies up to ~10 to 100 keV [*DeForest and McIlwain*, 1971; *Gabrielse et al.*, 2014]. These anisotropic electrons generate the electromagnetic chorus waves [*Tsurutani and Smith*, 1977; *Tsurutani et al.*, 1979, 2009; *Inan et al.*, 1978; *Meredith et al.*, 2002] through a temperature anisotropy/loss cone instability [*Brice*, 1964; *Kennel and Petschek*, 1966; *Tsurutani and Lakhina*, 1997]. The chorus then interacts with the ~100 keV electrons, accelerating them to relativistic MeV energies [*Horne and Thorne*, 1998; *Miyoshi et al.*, 2003; *Meredith et al.*, 2001, 2003a; *Omura et al.*, 2008; *Reeves et al.*, 2013; *Thorne et al.*, 2013; *Boyd et al.*, 2014]. This is the well-accepted overall scenario for relativistic electron acceleration at this time [*Tsurutani et al.*, 2006, 2010; *Kasahara et al.*, 2009; *Miyoshi et al.*, 2013; *Hajra et al.*, 2015a, 2015b].

It has recently been shown that high-speed streams (HSSs) and embedded Alfvén waves that cause High-Intensity Long-Duration Continuous AE Activity (HILDCAA) events [*Tsurutani and Gonzalez*, 1987; *Tsurutani et al*., 1995, 2004; *Hajra et al*., 2014a, 2014b] have a one-to-one association with relativistic electron acceleration events [*Hajra et al*., 2015a, 2015b]. This result is in strong support of the general scenario.

The relativistic electron decreases/dropouts (REDs) from the Earth's magnetosphere is also a well-known and long studied phenomenon [*Freeman*, 1964; *Imhof and Gaines*, 1993; *Baker et al*., 1994; *Gaines et al*., 1995; *Friedel et al*., 2002; *Onsager et al*., 2002; *Meredith et al*., 2006, 2011; *Clilverd et al*., 2006, 2016; *Borovsky and Denton*, 2009; *Horne et al*., 2009; *Morley et al*., 2010; *Turner et al*., 2014a]. This particle loss (REDs) is the focus of this paper.

There are two possible sinks for the relativistic electrons: the atmosphere and the magnetopause. The loss to the atmosphere is due to wave-particle cyclotron resonant interactions [*Thorne and Kennel*, 1971]. Energetic particles that are pitch angle scattered by plasma waves have some particles which enter the loss cone. These particles have mirror points deep in the atmosphere and thus have collisions with atmospheric atoms and molecules. These "precipitating particles" lose most of their primary energy by collisions with neutrals (to be described in detail later).

Thorne and Kennel [1971] and *Horne and Thorne* [1998] [see also *Bortnik et al*., 2006; *Millan and Thorne*, 2007; *Jordanova et al*., 2008; *Borovsky and Denton*, 2009; *Turner et al*., 2014b] have suggested the mechanism of pitch angle scattering by electromagnetic ion cyclotron (EMIC) waves and loss to the auroral atmosphere. *Miyoshi et al*. [2008] have shown a case of relativistic electron precipitation in an isolated proton aurora substantiating the existence of this mechanism. The EMIC waves were concluded to cause the precipitation of both the tens of keV protons and the relativistic electrons.

The loss of particles penetrating the magnetopause is called "magnetopause shadowing" (the phrase coined by *West et al*. [1972]). Energetic charged particles in the nightside magnetosphere will drift to larger *L* on the dayside due to drift-shell splitting [*Dessler and Karplus*, 1961; *Roederer and Zhang*, 2014]. This is the physical basis for magnetopause shadowing. Particles that penetrate the dayside magnetopause will be lost to the magnetosheath and will be convected downstream with the sheath plasma and fields [*Bortnik et al*., 2006].

There are at least three different interplanetary and magnetospheric cases where particle losses occur by magnetopause shadowing: enhanced solar wind pressure, particle radial diffusion in the magnetosphere, and magnetospheric inflation during magnetic storms. We will describe each one briefly.

When the dayside magnetosphere is compressed by high solar wind speeds or high plasma densities, or both, drift-shell splitting of charged particles becomes enhanced. This is one possible loss mechanism of the magnetospheric relativistic electrons [*Bortnik et al*., 2006].

The concept of particle radial diffusion by ULF waves that break the particle's third adiabatic invariant was first discussed by *Kellogg* [1959] and *Vernov et al*. [1960]. Resonant particles "diffuse" to both higher and lower *L* by this process. The particles that diffuse to larger *L* may drift to the magnetopause and be lost there [*Albert*, 2014]. In support of this, *Rae et al*. [2012] have determined that during enhanced solar wind speeds (e.g., enhanced ram pressures) magnetospheric ULF power is enhanced. *Shprits et al*. [2006, 2012] found that relativistic electron flux depletions occurred when the magnetopause was compressed and geomagnetic activity was high. Outward radial diffusion modeling using *Kp* as a proxy was performed by *Brautigam and Albert* [2000] for the 9 October 1990 storm with some success. See also *Hudson et al*. [2014]. *Dimitrakoudis et al*. [2015] found that *Kp* was the best parameter that specified ULF wave power.

A third scenario for relativistic electron losses by magnetopause shadowing was presented by *Kim and Chan* [1997]. They examined a storm time expansion of the magnetosphere conserving all three adiabatic invariants. Assuming a $Dst \leq -100$ nT storm main phase maximum, their model was able to cause a relativistic electron flux decrease of up to 2 orders of magnitude through magnetospheric inflation and magnetopause shadowing. Some more recent works on this loss process can be found in *Kim et al*. [2008, 2010]. It should be mentioned, however, that in our following study, we will be avoiding magnetic storm intervals, so this particular mechanism for REDs will not be applicable. We mention it here only for completeness.

The ratio of the two loss processes, wave-particle interactions, and magnetopause shadowing are different for different particle energies, particle pitch angles, L shells, plasma wave modes, frequencies, and intensities, and under different interplanetary and magnetospheric conditions.

Section 2 of this paper describes the data used, method of analyses and pertinent interplanetary structure background for the reader. Section 3 discusses the interplanetary causes of the REDs in the absence of geomagnetic storms. We specifically avoided storm intervals in this study so that possible electron injection and acceleration into the magnetosphere with energies $E > 100$ keV should be less important in general, while adiabatic dropouts discussed by *Kim and Chan* [1997] should be absent. Section 4 will show a case of EMIC and chorus waves under a solar wind compression event. A specific (new) property of the EMIC waves for scattering of relativistic electrons will be discussed. Consequences of wave-particle cyclotron resonant interactions between the electrons and EMIC waves will be explored. Section 5 gives the results of a calculation of the total energy of the relevant relativistic electrons existing within the outer magnetosphere ($L > 6$) prior to the REDs. This section also provides quantitative estimates of maximum energy deposition into the atmosphere at different altitudes using the GEANT4 simulation code. Section 6 is a summary of the results. Section 7 is the discussion section. Section 8 contains further discussion of other models/results pertaining to REDs, and section 9 is our conclusions concerning the possible relevance of our results to decreased area of high-vorticity centers at 300 mb altitudes (the *Wilcox et al*. [1973] effect), the *Tinsley and Deen* [1991] global circuit model, and other possible atmospheric effects. The paper makes a call for further efforts to use the numbers presented here to quantitatively examine a number of possible scenarios for climate change.

2. Data, Methods of Analyses, and Solar Wind Background

2.1. Data and Methods of Analyses

Solar wind/interplanetary data at 1 min time resolution were obtained from the OMNI website (http://omniweb.gsfc.nasa.gov/). OMNI interplanetary data had already been time-adjusted to take the solar wind convection time from the spacecraft to the Earth's bow shock into account. No further adjustment to the interplanetary data was made in this study.

The *AE* (1 min) [*Davis and Sugiura*, 1966] and *SYM-H* (1 min) [*Iyemori*, 1990] and *Dst* (1 h) geomagnetic indices were obtained from the World Data Center for Geomagnetism, Kyoto, Japan (http://wdc.kugi.kyoto-u.ac.jp). The *AE* (auroral electrojet) index is a superposition of the horizontal component of 12 or more longitudinally spaced ground magnetometers located in the auroral zone (~60° to ~70° magnetic latitude). The index gives a measure of the strength of the ionospheric current (auroral electrojet) that flows at ~100 km altitude. The *SYM-H* index measures the total energy of the radiation belt ~10–300 keV protons and electrons [*Dessler and Parker*, 1959; *Sckopke*, 1966].

HILDCAA intervals are identified using the *AE* and *SYM-H* indices. These intervals are defined by (1) peak $AE > 1000$ nT, (2) lasts > 2 days, (3) occurs outside of storm main phases, and (4) does not contain subintervals with $AE < 200$ nT for more than 2 h. For more details and examples, see *Tsurutani and Gonzalez* [1987], *Tsurutani et al*. [2006], *Guarnieri* [2006], and *Hajra et al*. [2013].

The integrated fluxes of relativistic > 0.6 and > 2.0 MeV electrons at geosynchronous orbit ($L = 6.6$) were taken by Geostationary Operational Environmental Satellites (GOES) GOES 8 and GOES 12 satellite particle instrumentation. The data website is http://www.ngdc.noaa.gov/stp/satellite/goes/dataaccess.html. For details of the particle instrumentation we refer the reader to *Onsager et al*. [1996].

The high time resolution (32 vectors/s) Cassini fluxgate magnetometer data were used for the EMIC wave analyses and the Cassini Radio and Plasma Wave Science (RPWS) search coil data were used to identify chorus waves. The Cassini magnetometer is described in *Southwood et al*. [2001], and the RPWS instrument is described in *Gurnett et al*. [1994].

The five vector/s Cluster magnetometer [*Balogh et al*., 2001] data were obtained from the Cluster Science Archive (CSA). The four vector/s magnetometer data from THEMIS [*Auster et al*., 2008] were obtained from the Space Physics Data Facility (SPDF) CDAWeb.

The wave polarization analysis is done using a minimum variance technique [*Sonnerup and Cahill*, 1967; *Smith and Tsurutani*, 1976]. The three high time resolution magnetic wave components are used to form a covariance matrix. The matrix is then diagonalized, and the wave fields are rotated into the new principal axis coordinate system. In this system B_1 is the wave field along the maximum variance direction, B_2 is along the intermediate variance direction, and B_3 is in the minimum variance direction. It has been shown by *Verkhoglyadova et al*. [2010] that the minimum variance direction is the wave propagation direction **k**.

Table 1. Eight HPS Pressure Pulse Events From SC23 That Were Not Followed by Magnetic Storms[a]

Number	Event	Start (DOY UT)	End (DOY UT)	Duration (h)	Peak Pressure (nPa)	HCS Time (DOY UT)
1	1995_150	150 02:39	150 05:37	3.0	26.6	150 04:44
2	1998_202	202 02:38	202 06:45	4.1	18.6	202 04:27
3	2000_027	027 14:04	027 21:35	7.5	20.3	027 18:03
4	2000_052	052 01:11	052 08:13	7.0	14.8	----
5	2003_258	258 16:32	259 03:16	10.7	8.0	258 20:43
6	2007_056	056 12:00	057 05:32	17.3	12.2	057 03:21
7	2007_243	243 13:43	243 20:52	7.2	5.1	243 21:37
8	2008_058	058 14:07	058 19:48	5.7	9.6	058 17:51

[a]All eight HPS impacts on the magnetosphere were associated with REDs.

For the study of EMIC wave occurrence on the ground, we use data from the Nagoya University Institute for Space-Earth Environmental Research (ISEE) magnetometer network (http://stdb2.isee.nagoya-u.ac.jp/magne/index.html). The locations of the highest magnetic latitude magnetometer site are in Athabasca, Canada at 61.7°N. We will use data from that station and from Moshiri, Japan, at 35.6°N. The magnetometers are identical induction magnetometers that have a turnover frequency of 1.7–5.5 Hz and sensitivity of 0.00810–1.3 V/nT at 0.1 Hz. The sampling rate of the magnetometer is 64 Hz [*Shiokawa et al*., 2010]. This magnetometer chain was started in 2005–2008 and is fully operating at present.

The energy deposition as a function of altitude for the relativistic electron precipitation was performed using the GEANT4 simulation package [*Agostinelli et al*., 2003] with a standard atmospheric target model [*Takada et al*., 2011; *Tanimori et al*., 2015]. The atmospheric model is the Japan Industrial Standard based on the International Standard Atmosphere ISO 2533-1975. GEANT4 was initially developed by European Organization for Nuclear Research to estimate high-energy particle interactions with materials such as detectors but has now much wider applications as will be shown in this paper [see also *Schröter et al*., 2005; *Wissing and Kallenrode*, 2009; *Artamonov et al*., 2016]. In the simulations performed, the primary electrons have monochromatic energies of 0.6, 1.0, and 2.0 MeV and are precipitated vertically downward from an altitude of ~630 km. In the range from 630 km to 80 km, the column density of the atmosphere was assumed to be 10^{-2} g cm^{-2}. Below 80 km the atmosphere was divided into 80 layers. The pressure and density of each layer was defined with a precision of better than 5%. The GEANT4 code includes Rayleigh-scattering, Compton-scattering, photon absorption, gamma ray pair production, multiple scattering, ionization, bremsstrahlung for electrons and positrons, and annihilation of positrons. Since we are considering near-polar regions for this precipitation, the terrestrial magnetic fields are considered to be vertical to the ground.

We first examine intervals of slow speed interplanetary streams that precede HSSs identified by *Hajra et al*. [2013]. We will only use events that occurred during solar cycle 23 (SC23) which were devoid of magnetic storms (events with *SYM-H* < -50 nT) [*Gonzalez et al*., 1994] following the slow streams. This selection was made so that there would be adequate high-resolution data available (the SC23 time interval) and no contamination due to magnetic storm energization processes. There were eight such events when $E > 0.6$ and > 2.0 MeV electron fluxes were available. All eight of these events are used in this study. A listing is given in Table 1.

2.2. Background on Solar Wind Structures

For this study we have used solar wind intervals that contain the heliospheric current sheet (HCS) and the adjacent high-density heliospheric plasma sheet (HPS) crossings that precede the HSS proper. The discovery paper for the HCS was *Smith et al*. [1978], and for a HPS description, see *Winterhalter et al*. [1994].

Figure 1 illustrates the relationship between the slow solar wind and the fast solar wind detected at 1 AU. Such structures are typically detected in the declining phase of the solar cycle. The solar wind speed is shown in Figure 1 (third panel). The slow solar wind is on the left, and the fast solar wind or HSS is on the right. Where the fast solar wind overtakes the slow solar wind, an interaction region called the corotating interaction region or CIR [*Smith and Wolfe*, 1976] forms. The CIR is indicated by the high plasma densities (Figure 1, first panel), high magnetic field intensities (Figure 1, second panel), and high plasma temperatures (not shown). High-speed streams (HSSs) typically "sweep up" the heliospheric current sheet (HCS) and the heliospheric plasmasheet (HPS), so these structures occur ahead of the high-speed stream proper. The HCS is indicated by the vertical dashed line, and the HPS is the high-density region adjacent to the HCS.

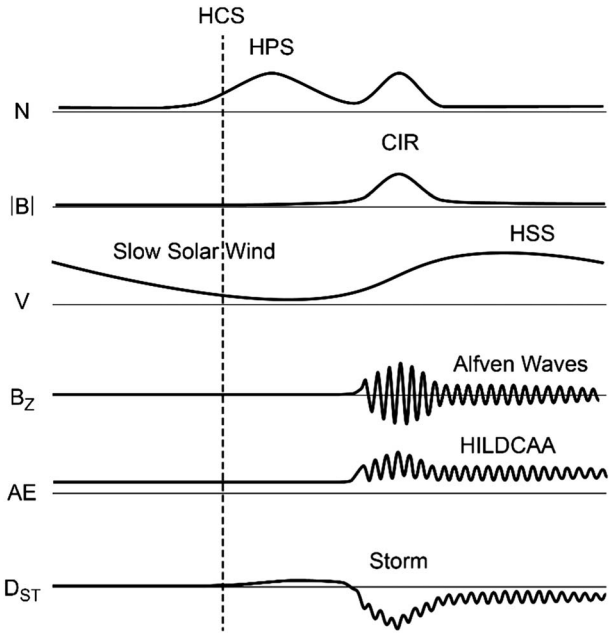

Figure 1. A schematic of the region near the slow stream-high-speed stream interaction. (first panel) The solar wind density *N*, (second panel) the interplanetary magnetic field magnitude |*B*|, (third panel) the solar wind velocity *V*, (fourth panel) the interplanetary magnetic field B_z component, and the (fifth panel) geomagnetic *AE* and (sixth panel) *Dst* indices. The dashed vertical line is the heliospheric current sheet (HCS), and the density associated with it (asymmetrically on the right side) is the heliospheric plasma sheet (HPS). A corotating active region (CIR) and HSS HILDCAAs are shown for context. They are present sunward of the HPS and impact the Earth's magnetosphere after the HPS impact in time.

The heliospheric current sheet is a region where the polarity of the interplanetary magnetic field (IMF) reverses polarity, i.e., from an inward polarity to an outward one, or vice versa. The standard convention [*Ness and Wilcox*, 1964] is that an outward IMF polarity is one where the interplanetary magnetic field is positive outward from the Sun. In either GSM or GSE coordinates, this is a negative B_x value. Since the interplanetary magnetic field is wound in a Parker/Archimedean spiral which has a ~45° angle relative to the Sun-Earth line at 1 AU, a positive polarity interplanetary magnetic field will have a negative B_x value and a positive B_y value. A negative polarity interplanetary magnetic field conversely will have a positive B_x value and a negative B_y value. A heliospheric current sheet crossing is therefore identified by a reversal of both B_x and B_y values.

It should be noted that the old name for the "heliospheric current sheet" [*Smith et al*., 1978] is "sector boundary" [*Ness and Wilcox*, 1964]. When the interplanetary polarity structures were first discovered by satellite measurements in the ecliptic plane, it was noted that there were an even number of polarity reversals per solar rotation: 2, 4, or 6. This indicated that the Sun's magnetic field might have dipolar, quadrupolar, or octupolar components. It was not until the Pioneer 11 spacecraft went out of the ecliptic plane during a solar minimum phase that it was realized that there was only one main current sheet [*Smith et al*., 1978], much like the theoretically envisioned *Alfvén* [1977] flapping "ballerina skirt." The HCS is accompanied by high-density cold plasma, typical of the slow solar wind. The cold plasma adjacent to the HCS has been called the HPS. It should be noted that both the HCS and HPS are typically part of the slow solar wind. The HCS and HPS occur prior to the CIR and HSS as indicated in Figure 1.

3. Results: Particles

3.1. Relativistic Electron Dropouts (REDs)

3.1.1. Days 201 to 208, 1998

Figure 2 shows a relativistic electron ($E > 0.6$ and $E > 2.0$ MeV) flux dropout event beginning on day 202 of 1998. From Figures 2 (first panel) to 2 (ninth panel), the panels show the $E > 0.6$ MeV and $E > 2.0$ MeV electron fluxes ($cm^{-2}\,s^{-1}\,sr^{-1}$), the solar wind speed (V_{sw} in $km\,s^{-1}$), the solar wind density (N_{sw} in cm^{-3}), the solar wind ram pressure (P_{sw} in nPa), the interplanetary magnetic field magnitude (IMF B_0 in nT), and the B_x, B_y, and B_z components (nT) in GSM coordinates. Figures 2 (tenth panel) to 2 (eleventh panel) give the *SYM-H* (nT) and *AE* (nT) geomagnetic indices. There are two black vertical lines in the figure, one at ~0307 UT on day 202 and a second at ~0950 UT on day 205. These correspond to the times of flux dropout and recovery, respectively.

There is a red vertical line in Figure 2 which is located at ~0419 UT on day 202. This corresponds to a HCS crossing. The crossing is identified by the sudden changes in the IMF B_x component sign (from a

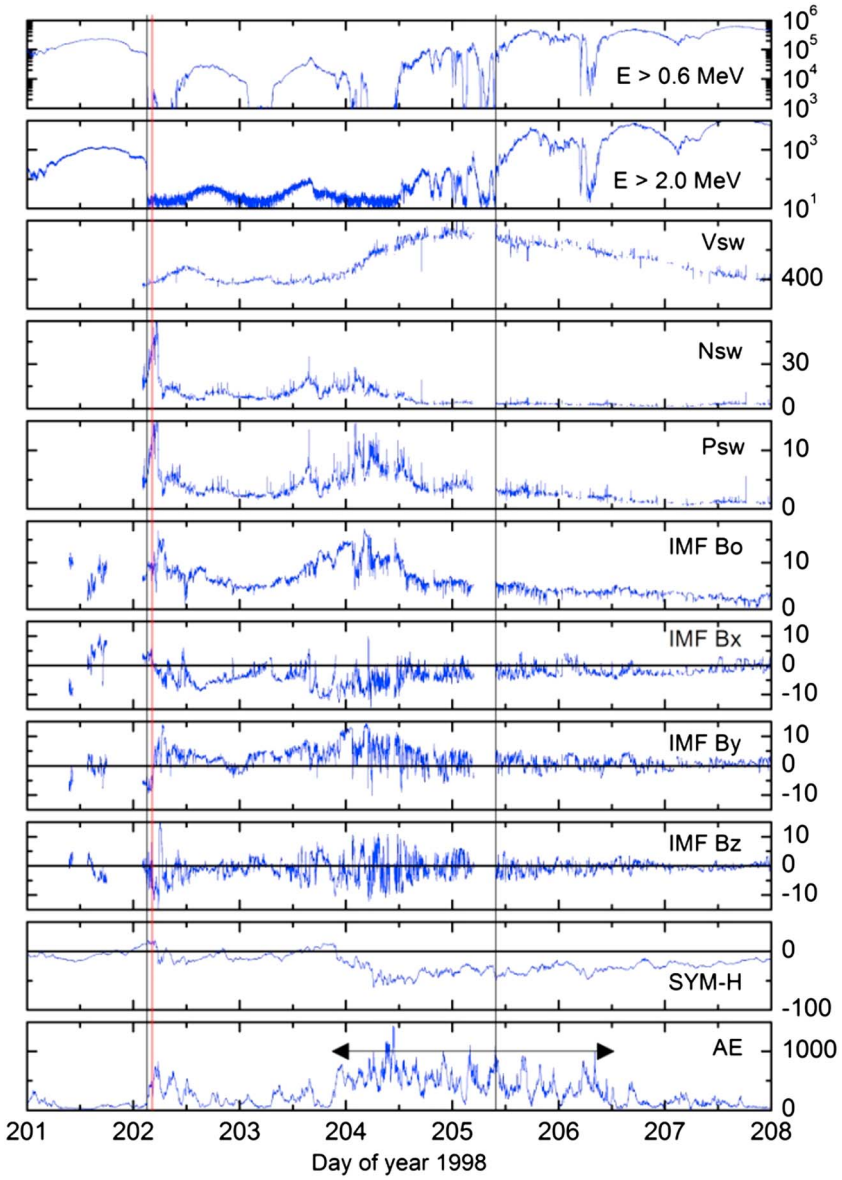

Figure 2. A relativistic electron ($E > 0.6$ MeV and $E > 2.0$ MeV) flux dropout event from day 202 to 206, 1998. The (first panel) $E > 0.6$ MeV and (second panel) $E > 2.0$ MeV electron fluxes ($cm^{-2}\,s^{-1}\,sr^{-1}$), (third panel) the solar wind speed (V_{sw} in km s^{-1}), (fourth panel) the solar wind density (N_{sw} in cm^{-3}), (fifth panel) the solar wind ram pressure (P_{sw} in nPa), (sixth panel) the interplanetary magnetic field magnitude (IMF B_0 in nT), and the (seventh panel) B_x, (eighth panel) B_y, and (ninth panel) B_z components (nT) in GSM coordinates. The (tenth panel) *SYM-H* (nT) and (eleventh panel) *AE* (nT) geomagnetic indices. The onset and recovery are indicated by vertical black lines, respectively. The HCS is indicated by a vertical red line. The HILDCAA interval is given by a horizontal arrow in the bottom.

positive value to a negative value) with a simultaneous change in the IMF B_y sign (from a negative value to a positive one). Thus, from the standard convention of *Ness and Wilcox* [1964], the interplanetary magnetic field switched from a "negative (inward) polarity" to a "positive (outward) polarity" Parker spiral magnetic field.

The vertical black line slightly to the left of the HCS is time coincident with a sudden decrease in the $E > 0.6$ and $E > 2$ MeV electron fluxes from 8.4×10^4 particles $cm^{-2}sr^{-1}\,s^{-1}$ to ~25 particles $cm^{-2}\,sr^{-1}\,s^{-1}$ and from ~4.6×10^2 particles $cm^{-2}sr^{-1}\,s^{-1}$ to ~8 particles $cm^{-2}sr^{-1}\,s^{-1}$, respectively. The $E > 0.6$ MeV fluxes decreased by ~8.4×10^4 particles $cm^{-2}sr^{-1}\,s^{-1}$, and the $E > 2.0$ MeV fluxes decreased by ~4.5×10^2 particles $cm^{-2}sr^{-1}\,s^{-1}$, respectively. These decreases occur within ~1.7 h and 1.0 h, respectively.

The electron flux dropouts are time coincident with the onset of an interplanetary high-density (N_{sw}) plasma feature. The plasma density rise started at ~0238 UT and lasted until ~0645 UT on day 202. The peak density reaches ~62 cm^{-3} at 0506 UT. The pressure pulse rise started at ~0238 UT and then more-or-less monotonically increased to the maximum value of ~19 nPa at 0512 UT on day 202. The pressure slowly decreased to ~6 nPa by ~0645 UT. The pressure increase was slow and gradual and took almost ~3 h to go from the base value to the peak value. A positive *SYM-H* peak value of ~ +20 nT occurs at the time of highest ram pressure. Because the *SYM-H* index increased slowly with time, this event was not a sudden impulse (SI^+) such as is caused by an interplanetary shock (for examples of shock induced SI^+ events, we refer the reader to *Tsurutani et al*. [2008]). This positive *SYM-H* is typical of the slow solar wind and was indicated in Figure 1. Although the $E > 0.6$ and $E > 2.0$ MeV electron flux dropouts were abrupt, the HPS density feature was slow and long lasting. The location of the plasma density feature being adjacent to the HCS identifies it as the heliospheric plasmasheet or HPS.

The HCS and the HPS occurred in the slow solar wind. The V_{sw} at this time was only ~380 km s^{-1}. It is thought that both of these interplanetary structures are associated with the outward flow of material from solar helmet streamers [*Hundhausen*, 1977; *Suess and Nerney*, 2001]. Even though the HPS density was in a low solar wind speed interval, the P_{sw} associated with it was ~19 nPa, the highest value of the entire interval displayed in the figure. The HCS and the HPS of Figure 2 follows the schematic of Figure 1 quite well.

The geomagnetic activity level was weak throughout the period when the electron fluxes were decreasing. *AE* reached a peak value of ~836 nT at ~0538 UT on day 202 and then decreased with time thereafter. This relatively low-intensity *AE* was most likely due to the stimulated release of stored magnetotail energy in the form of a substorm [*Zhou and Tsurutani*, 2001; *Tsurutani et al*., 2006]. It should be noted that substorms have much less total energy than magnetic storms [*Gonzalez et al*., 1994]. Substorms are thought to be an elemental part of magnetic storms, thus the name [*Akasofu*, 1964].

The CIR [*Smith and Wolfe*, 1976; *Pizzo*, 1985; *Tsurutani et al*., 2006] created by the following HSS-slow speed stream interaction occurs much later in time. The HSS occurs between ~1200 UT on day 203 and ~1850 UT day 204. There is no magnetic storm associated with the CIR in this case. The lowest value of *SYM-H* was −48 nT, and this was reached at ~1500 UT on day 204, just in the trailing portion of the CIR. The relativistic electron flux remains low throughout this CIR high ram pressure interval.

3.1.2. Days 56 to 64, 2007

A second example of a RED is shown in Figure 3 for a 2007 event. The format of the figure is the same as used in Figure 2. The $E > 0.6$ MeV and $E > 2.0$ MeV relativistic electron flux decreases both started at ~1647 UT on day 56 (indicated by a vertical black line) and reached minimum values at ~0220 UT day 57. The $E > 0.6$ MeV flux decreased from ~2.5×10^4 to ~3×10^2 particles $cm^{-2}\,s^{-1}\,sr^{-1}$. The $E > 2.0$ MeV flux decreased from ~9×10^2 to ~9 particles $cm^{-2}\,s^{-1}\,sr^{-1}$. The flux decreases were thus ~2.5×10^4 particles $cm^{-2}\,s^{-1}\,sr^{-1}$ for the $E > 0.6$ MeV electrons and ~9×10^2 particles $cm^{-2}\,s^{-1}\,sr^{-1}$ for the $E > 2.0$ MeV electrons. This RED was ~9.5 h in duration considerably longer than the event in Figure 2.

The HCS is denoted by the red vertical line where the IMF B_x component changed from ~ +2.8 nT to −5.8 nT and the IMF B_y simultaneously reversed sign from −12.3 nT to +6.9 nT. This occurs at ~0321 UT on day 57. This was a switch from a negative interplanetary magnetic field polarity to a positive polarity.

For the event shown in Figure 3, the HPS was composed of high-density plasma regions on both sides of the HCS. The HPS started at ~1200 UT on day 56, rose gradually until ~2000 UT when the increase became more abrupt. It reached a peak value of ~6.1 nPa at 0030 UT on day 57, then decreased slightly at the HCS, and then increased again. The ram pressure reached a maximum value of ~12 nPa at ~0301 UT on day 57 and ended at ~0532 UT on day 57. The relative electron flux dropout coincides with the HPS event. The ram pressure associated with the HPS impingement onto the magnetosphere was again gradual with the whole event lasting ~17 h.

The geomagnetic activity throughout the interval was relatively weak. The HPS pressure stimulated an *AE* peak of ~420 nT at most a very small substorm. *AE* following the HPS pressure pulse was ~9 nT from ~1200 UT on day 57 through ~0630 UT on day 58. The *SYM-H* index reached a peak value of +12 nT at ~0312 UT. This occurred roughly at the center of the HPS event.

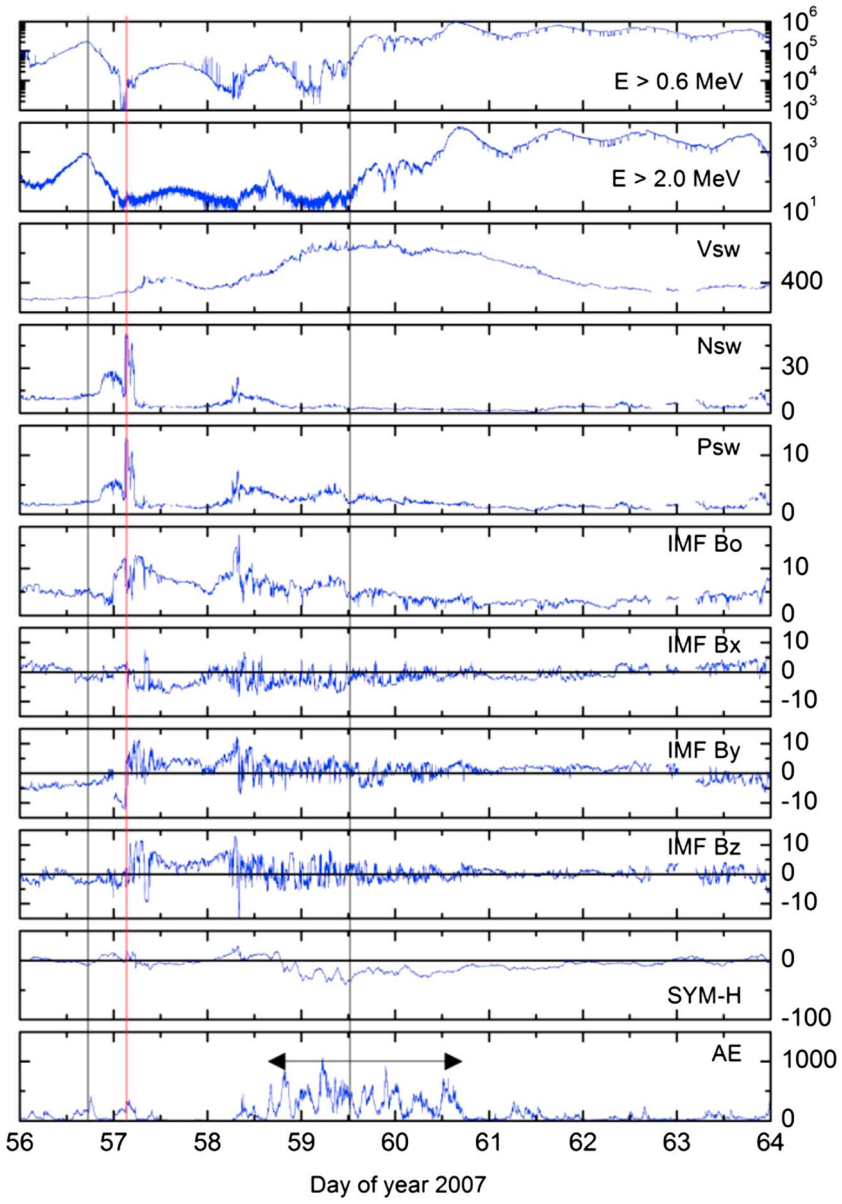

Figure 3. $E > 0.6$ and $E > 2.0$ MeV relativistic electron flux dropout event from day 56 to day 59, 2007. The format is the same as in Figure 1. The dropout is present in the interval between the solid vertical black lines. The HCS in indicated by the vertical red line.

The CIR was present from ~0000 UT day 58 to ~0000 UT day 59. Because the IMF was mostly northward within the CIR, no magnetic storm occurred.

Tables 1 and 2 give a listing of all eight HPS/RED events studied. Table 1 gives the information on the associated interplanetary parameters, and Table 2 gives the relativistic electron flux information. The events are listed in chronological order with the one shown in Figure 2 as event 2 and the one in Figure 3 as event 6 in the tables.

In Table 1, the columns from left to right are as follows: the number of the event, the pressure pulse year and day (DOY), the start time in UT, the end time, the peak pressure in nPa, and the time of the HCS crossing. The events occurred between the years 1995 and 2008. As previously mentioned all events occurred in SC23. The duration of the pressure pulses range from ~3.0 h (event 1: 1995 event) to 17.3 h (event 6: 2007 DOY 057), with a mean duration of 7.8 h. The pressure pulse peaks range from 5.1 nPa (event 7: 2007 DOY 243) to 26.6 nPa (event 1). The mean peak pressure for the eight events is 15.3 nPa. All pressure pulse events were HPSs adjacent to HCS crossings.

Table 2. Relativistic Electron Flux Dropouts

Number	Event	Electron Dropout (DOY UT) Start	Electron Dropout (DOY UT) End	GOES LT at Dropout Start (DOY UT)	Flux Before Dropout ($cm^{-2}\,s^{-1}\,sr^{-1}$) E1 ($\times10^4$)	Flux Before Dropout ($cm^{-2}\,s^{-1}\,sr^{-1}$) E2 ($\times10^2$)	Flux at Dropout ($cm^{-2}\,s^{-1}\,sr^{-1}$) E1	Flux at Dropout ($cm^{-2}\,s^{-1}\,sr^{-1}$) E2
1	1995_150	150 03:08	150 04:15	149 22:10	4.1	5.0	19	7
2	1998_202	202 01:59	202 03:38	201 21:01	8.4	4.6	25	8
3	2000_027	027 16:34	027 17:28	027 11:34	3.1	2.0	62	3
4	2000_052	051 20:06	052 06:47	051 15:04	7.2	3.9	68	5
5	2003_258	258 22:00	259 08:38	258 17:00	21.1	27.9	14	12
6	2007_057	057 01:03	057 02:23	056 20:03	2.5	8.8	296	9
7	2007_243	244 06:40	244 07:59	244 01:41	2.7	21.6	38	13
8	2008_058	058 19:00	059 05:46	058 14:01	15.8	17.7	61	13

Table 2 contains the relativistic electron flux values prior to the dropout and after the dropout, for the two energy channels. The columns are from left to right: the event number, event year and day, the $E > 0.6$ MeV dropout start time and end times in UT, and the E1 (>0.6 MeV) and E2 (>2.0 MeV) electron fluxes before the dropout and at the dropout.

All of the HPSs were time coincident with the onset of the relativistic electron flux dropouts. The HPSs were all in the slow solar wind. The $E > 0.6$ MeV flux decreases ranged from 2.1×10^5 to 2.5×10^4 particles $cm^{-2}\,s^{-1}\,sr^{-1}$, with a log average of 5.9×10^4 particles $cm^{-2}\,s^{-1}\,sr^{-1}$. For the $E > 2.0$ MeV fluxes, the decreases ranged from 2.8×10^3 to 2×10^2 particles $cm^{-2}\,s^{-1}\,sr^{-1}$ with a log average of 5.6×10^2 particles $cm^{-2}\,s^{-1}\,sr^{-1}$. The dropout time durations can be as short as 1 h (see events 1–3, 6, and 7).

The peak ram pressures ranged from 5.1 to 26.6 nPa with an average of 15.3 nPa. The time durations of the HPSs were 3.0 to 17.3 h with an average of 7.8 h.

It should be noted that the two events that were explicitly shown (Figures 2 and 3) have flux dropouts at the intermediate levels; neither the highest nor the lowest decreases in flux. Event 5 has initial fluxes a factor of ~3 times higher than the event in Figure 2. For sample calculations which we will perform later in the paper, we will use a ~10^5 particles $cm^{-2}\,s^{-1}\,sr^{-1}$ flux decrease in the $E > 0.6$ MeV energy range. For the $E > 2$ MeV electrons we will use a flux decrease value of ~10^3 particles $cm^{-2}\,s^{-1}\,sr^{-1}$. One can note from Table 2 that this is near the upper end of the measurements but not the maximum.

3.2. Relativistic Electron Spectra

Figure 4 shows the two-point predropout flux spectra for all eight events listed in Table 2. The separate spectra are the connected lines indicated in blue. Although the individual events are not labeled in the graph, the fluxes given in Table 2 can be used to identify them if desired. The red line is the log average of the eight values.

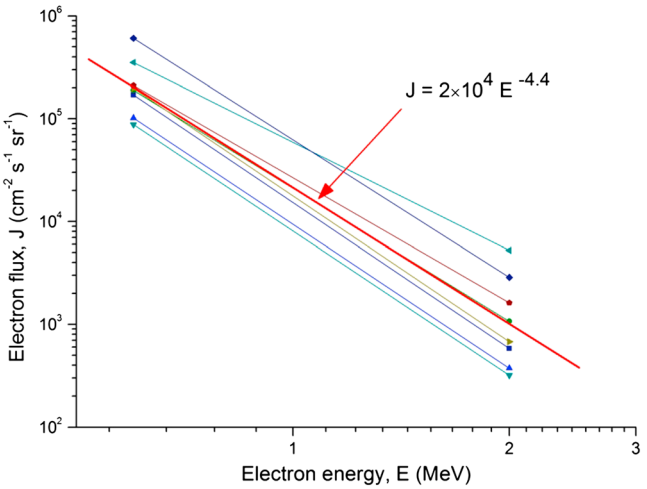

Figure 4. A fit to the eight relativistic electron predropout flux power spectra.

If we assume that the energy flux spectrum follows a straight line in logarithm space, then the average flux spectrum (the red line) has a power law spectral shape with $J = 2\times10^4\,E^{-4.4}\,cm^{-2}\,s^{-1}\,sr^{-1}$. The −4.4 exponential of the power law indicates that the spectrum is very steep; e.g., the relativistic electrons within the magnetosphere are primarily confined to the low-energy range.

4. Results: Emic Waves

4.1. Background

Electomagnetic ion cyclotron (EMIC) waves are left-hand (LH) polarized

waves generated by a plasma instability associated with anisotropic $T_{\perp}/T_{||} > 1$ energetic protons [*Cornwall*, 1965; *Kennel and Petschek*, 1966]. These waves have been shown by spacecraft observations to be generated in the dayside outer magnetosphere associated with solar wind pressure pulses [*Anderson and Hamilton*, 1993; *Engebretson et al*., 2002; *Usanova et al*., 2012]. *Olson and Lee* [1983] earlier noted that PC1 waves were detected at the ground during sudden impulses (SI^{+}s). The authors' interpretation was that the shock compression of the magnetosphere was most effective in (betatron) accelerating energetic protons near noon just inside the magnetopause. *Anderson and Hamilton* [1993] suggested that remnant energetic protons existing near the dayside magnetopause are marginally stable and small solar wind ram pressure increases could easily cause the growth of EMIC waves.

EMIC waves were sought for the eight interplanetary pressure pulse events listed in Tables 1 and 2. The results of the search are given in Table A1. We have searched the ESA-NASA Cluster data [*Escoubet et al*., 2001; *Balogh et al*., 2001] and the NASA THEMIS data [*Angelopoulos et al*., 2008; *Auster et al*., 2008] for the 2000 to 2008 events (events 3–8). Unfortunately, Cluster was launched in day 235, 2000, after events 3 and 4. THEMIS continuous data are available from March 2007, after event 6. For events 5 and 7, Cluster was on the nightside (~2324 and ~0116 LT) of the magnetosphere, respectively. For event 6, Cluster was near local noon (~1235 LT) but was ~11 R_E away from the magnetic equator. For event 8, Cluster was inside the morningside (~0847 LT) plasmasphere. The Cluster instrumentation did not detect EMIC waves in this case. THEMIS was in the morningside (~0843 LT) magnetosheath during event 7. For event 8, THEMIS was not in the outer magnetosphere.

We thus did not detect any EMIC waves during the eight pressure pulse events either in the Cluster data or in the THEMIS data. It is suspected that the lack of wave detection was due to (a) the lack of spacecraft data (events 1–4) and (b) the spacecraft being at a local time or L shell where EMIC waves are not expected to be generated (events 5–8). So for all eight pressure pulse events, we were unlucky to not have plasma wave data on the dayside outer region of the magnetosphere near the wave generation region. We did a similar search with Geotail and again found that the satellite position at the time of our eight events was not compatible with EMIC wave detection in the dayside outer zone magnetosphere.

Although we do not have an EMIC wave event during any of the eight pressure pulse events in either Cluster or THEMIS or Geotail data sets due to unfortunate spacecraft locations, we noted previously that *Anderson and Hamilton* [1993], *Engebretson et al*. [2002], and *Usanova et al*. [2012] have shown EMIC wave generation by solar wind pressure pulses. *Park et al*. [2016] has recently done a comprehensive statistical study of EMIC waves for $Kp < 1$. Their results clearly indicate that EMIC waves are generated in the outer dayside magnetosphere due to solar wind pressure enhancements. The local time of the waves was centered near 1100–1200 local time, as one would expect for solar wind compression.

Solar wind pressure pulse such as fast shocks have been shown to cause dayside auroras with the auroras first starting at local noon and then expanding to both dawnside and duskside [*Craven et al*., 1986; *Zhou and Tsurutani*, 1999; *Tsurutani et al*., 2001; *Zhou et al*., 2003, 2009]. The auroras are presumed to be caused by shock compression of the magnetosphere with perpendicular (to the magnetic field) acceleration of preexisting ~10 to 100 keV ions and electrons, generation of EMIC waves and chorus, and pitch angle scattering of both particle species and loss to the ionosphere. So far no shock event has been shown that does not have a corresponding dayside aurora.

Although we are missing EMIC wave detection for our eight HPS events because of unfortunate spacecraft locations, we do have ground based magnetometer events and a Cassini wave event to show and analyze. Two ground observations actually occurred simultaneously with the dropout events 6 and 8 previously discussed in Tables 1 and 2. The second observation has the advantage that Cassini flew into the magnetosphere at almost along the Sun-Earth line, rapidly sampling a variety of L shells during a short time interval. We will show that during solar wind pressure pulses EMIC waves and simultaneous chorus wave events are detected in the dayside outer magnetosphere, as expected theoretically. We will further show that the EMIC waves are coherent, a topic that will be discussed further below.

4.2. Cassini Dayside EMIC Waves

The Cassini spacecraft passed through the outer region of the dayside magnetopause almost along the Sun-Earth line on 18 August 1999 during its Earth flyby. Cassini crossed the magnetopause at $L \sim 10.0$ at ~1300 local time (LT). The magnetopause crossing is indicated by the broadband noise observed in the

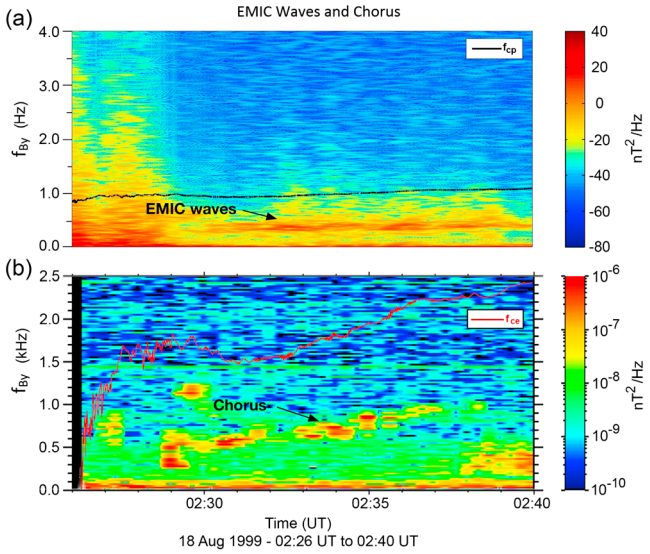

Figure 5. (a) The dynamic power spectrum for the EMIC waves from the Cassini magnetometer instrument and (b) the chorus from the Cassini RPWS instrument. The solid lines are the local proton gyrofrequency (in black) and electron gyrofrequency (in red), respectively.

spectrum at ~0332 UT. The satellite traveled near the magnetic equator from 3.1° to 1.5° in magnetic latitude (MLAT) and local time from 1259 to 1312 MLT as it went from L = ~10.0 to ~7.0. This outer portion of the dayside magnetosphere is presumably the wave generation region, where the magnetospheric magnetic field is the weakest. During the spacecraft passage there was an enhanced solar wind compression of the magnetosphere [*Tsurutani et al.*, 2002; *Remya et al.*, 2015]. The highest pressure of this event was associated with a CIR on days 15–16 August (peak pressure of ~16 nPa). This wave interval is in the high-speed stream proper as the pressure was still high but decreasing. At 0100 UT the pressure was ~2.1 nPa just prior to the interval shown.

The Cassini near-Earth encounter (done for a gravitational assist) is unique and cannot be duplicated by Earth-orbiting spacecraft. The satellite was continuously at a location near the magnetic equator at a variety of L shells where both EMIC and chorus waves will be generated. The encounter was also at a time of a high-speed stream where the magnetosphere was compressed.

Figure 5a shows the dynamic spectrum of the B_y component of waves detected during 0226 to 0240 UT on 18 August 1999. The black line indicates the local proton cyclotron frequency. The magnetic spectral density is shown by a legend on the right. The waves are electromagnetic, left-hand polarized (not shown to conserve space) and have frequencies below the local proton cyclotron frequency, thus confirming that these waves are indeed EMIC waves. The EMIC waves end at the end of the figure, ~ 0240 UT. The EMIC waves span L = ~10 to ~7.

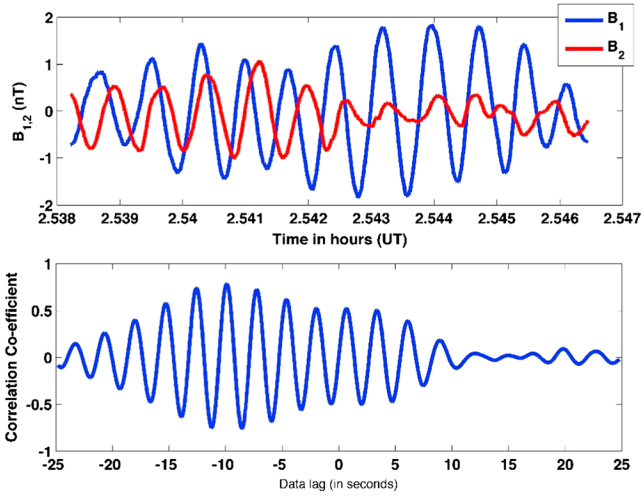

Figure 6. A packet of EMIC waves for the event shown in Figure 5. The top shows the magnetic component of the wave in minimum variance coordinates where B_1 is the maximum variance component and B_2 is the intermediate variance component. The bottom shows the cross correlation coefficient between B_1 and B_2 as a function of lag.

Figure 5b shows the higher-frequency waves detected during the pass. The solid red line is the electron cyclotron frequency. The waves in this panel are electromagnetic, are detected at frequencies below the electron cyclotron frequency, and are thus chorus whistler-mode waves. Chorus waves are present from ~0228 UT to ~0238 UT or from L = ~10 to ~7.5. Chorus is detected almost simultaneously with the EMIC waves.

Figure 6 shows a packet of the EMIC waves for the event shown in Figure 5. The packet occurred between 0232:17 and 0232:47 UT or a ~30 s interval. Figure 6 (top) shows that the waves begin as LH circularly polarized and then become more elliptically polarized. The wave period

is ~2.8 s (a power spectrum was calculated but is not shown to conserve space). Figure 6 (bottom) shows that during the circular polarization part of the packet, the cross correlation between the B_1 and B_2 components is high, close to 0.8. The high cross correlation indicates that the waves are quasi-coherent to coherent.

4.3. Coherent EMIC Waves and Relativistic Electron Pitch Angle Transport

An electron can cyclotron resonate with a wave when the wave is Doppler shifted to the particle's cyclotron frequency or its harmonics. The cyclotron resonance condition is given by the equation [*Kennel and Petschek*, 1966]:

$$\omega - k_{\parallel} v_{\parallel} = \frac{n\Omega}{\gamma} \tag{1}$$

where ω is the wave frequency and $k_{\parallel}$ and $v_{\parallel}$ are the wave vector **k** and particle velocity **v** component parallel to the ambient magnetic field $\mathbf{B}_0$, respectively. Here Ω is the electron cyclotron frequency, n is the harmonic number (=0, ±1, ±2, …). The relativistic factor $\gamma = (1 - v^2/c^2)^{-1/2}$ where v is the particle speed and c is the speed of light. Depending on whether n is positive/negative in equation (1), it represents the normal/anomalous cyclotron resonance condition [*Tsurutani and Lakhina*, 1997]. When n is negative, anomalous Doppler-shifted cyclotron resonance occurs. The particle is traveling in same direction as the wave along the magnetic field, and the waves will be Doppler shifted to the particle cyclotron frequency or its harmonics in the particle reference frame. The particles sense the waves to have a polarization opposite (thus the term "anomalous") to the plasma frame polarization. In the case we are considering here, relativistic electrons interacting with LH EMIC waves, the Doppler shift brings the wave frequency up to the electron cyclotron frequency, and because the electrons are overtaking the waves, they sense them as RH polarized, the same sense as electron rotation around B_0 [*Tsurutani and Lakhina*, 1997].

For the fundamental anomalous electron cyclotron resonance ($n = -1$) with a left-hand wave, equation (1) can be simplified for resonant particle velocity:

$$v_{\parallel} = v_{\parallel R} = v_{ph}(1 + \Omega/\omega\gamma) \tag{2}$$

where v_{ph} is the parallel wave phase speed. The relativistic parallel kinetic energy of the resonant electrons is thus given by *Kennel and Petschek* [1966] for incoherent waves:

$$E|| = \frac{\gamma m v_{\parallel R}^2}{2} = \frac{\gamma m v_{ph}^2}{2}\left(1 + {}^{\Omega}/_{\gamma\omega}\right)^2 \tag{3}$$

Electromagnetic ion cyclotron waves alter the particle pitch angle, (given by $\tan\alpha = v_{\perp}/v_{\parallel}$), when they are in cyclotron resonance with the wave. Here α is the angle between the particle velocity vector **v**, and the ambient field $\mathbf{B}_0$ and $v_{\perp}$ are the perpendicular components of the particle velocity with respect to $\mathbf{B}_0$.

The change $\Delta\alpha$ in particle pitch angle for arbitrary α is obtained as

$$\Delta\alpha = \frac{B}{B_0}\Omega\Delta t \tag{4}$$

and the pitch angle diffusion D is given by

$$D = \frac{\Delta\alpha^2}{2\Delta t} = \frac{\Omega}{2}\left(\frac{B}{B_0}\right)^2 \eta \tag{5}$$

where B is the wave magnetic field amplitude, Ω is the electron cyclotron frequency, and Δt is the interaction time between the electrons and the wave packet. When energetic particles cyclotron resonate with several cycles of the waves, the pitch angle transport in one short duration interaction can move the particle pitch up to 3 orders of magnitude faster than the quasi-linear diffusion rate [*Kennel and Petschek*, 1966].

We follow the calculations of *Remya et al.* [2015] for the details of relativistic ~0.9 MeV electrons interacting with a coherent EMIC wave packet shown in Figure 6. We assume that because the EMIC waves are coherent, the relativistic electrons stay in cyclotron resonance with two complete cycles of the wave [see *Lakhina et al.*, 2010; *Bellan*, 2013]. This is different from the *Kennel and Petschek* [1966] and *Tsurutani and Lakhina* [1997] approaches which assumed incoherent electromagnetic waves.

Table 3. Electron Anomalous Cyclotron Resonance With Two Cycles of an EMIC Wave of Conservative Amplitude 2.0 nT at a Variety of Different L Shells[a]

Parameters	$L=10$	$L=9$	$L=8$	$L=7$	$L=6$
V_{ph} (* 10^5 m/s)	2.2643	2.1946	2.3163	2.3732	3.499
Ωe (* 10^4 rad/s)	1.077	1.0873	1.2956	1.4756	3.4274
ω (rad/s)	3.107	2.255	2.6	3	3
$V_{\|\|}$ (* 10^8 m/s)	2.8025	2.886	2.9037	2.9057	2.9916
γ	2.8	3.66	3.98	4.019	13.37
$E_{\|\|}$ (MeV)	0.625	0.87	0.954	0.964	3.4
Δt (ms)	4.357	4.11	4.37	4.41	6.32
$\Delta\alpha$ (deg)	31.5	22.6	22.2	22.1	9.5
D (s^{-1})	34.65	18.87	17.08	16.85	2.18
T (ms)	28.9	53	58.5	59.3	457.8

[a]The rows, from top to bottom, are the wave phase velocity, the electron cyclotron frequency at the equator, the parallel speed of the electron along B_0, the parallel kinetic energy of the electron, the time of wave-particle interaction, the amount of particle pitch angle transport, the diffusion coefficient D, and the time for particle pitch angle diffusion T.

The wave is detected at $L=9$ and at a geomagnetic latitude 2.6°. We conservatively assume cyclotron resonance for only 2 out of the 11 wave cycles of the wave packet. The plasma parameters used are wave frequency $\omega=2.25$ rad/s, electron gyrofrequency $\Omega_e=1.08\times10^4$ rad/s, wave amplitude $B\sim2.0$ nT, and an ambient magnetic field of magnitude $B_0\sim62$ nT. For a wave phase speed $v_{ph}\simeq2.2\times10^5$ m/s, calculated numerically using the Waves in Homogeneous Anisotropic Magnetized Plasma code (WHAMP) [*Ronnmark*, 1982], the resonant electron parallel speed is determined to be $v_{\|}\simeq2.88\times10^8$ m/s.

The relativistic factor γ is 3.7. The wave packet spatial length X obtained as wave phase speed times the wave packet duration is therefore $X\simeq11.9\times10^5$ m. The interaction time between the electrons and the wave packet is calculated as X divided by the relative speed of the electrons with the wave packet, which is $\Delta t=4.1$ ms. The electron is hence pitch angle transported to $\Delta\alpha\sim23°$ in this single wave-particle interaction. The electrons are thus diffused at a rate $D=18.0\,s^{-1}$ in a time $T=1/D\simeq53$ ms.

Table 3 gives the results of a number of different L shells from 10 to 6. Please note that the electron parallel energy for resonance is $E<1$ MeV for the range from $L=10$ to $L=7$. It is only when we consider the case of $L=6$ that the resonant energy becomes >1.0 MeV.

The above calculations are only simple estimates. Exact nonlinear transport analyses in the presence of coherent EMIC waves would require a Green's function approach as was done for electromagnetic chorus [*Artemyev et al*., 2014; *Omura et al*., 2015]. The considered mechanism is expected to be especially efficient, due to the remarkable stability of electron trapping by intense coherent EMIC waves in the presence of various perturbations [*Artemyev et al*., 2015]. Still, it should be mentioned that EMIC waves mostly resonate with low to medium pitch angle electrons, up to 60° or so [*Summers and Thorne*, 2003; *Omura and Zhao*, 2013; *Kersten et al*., 2014; *Usanova et al*., 2014] which might prevent the precipitation of half of the electron population. However, it was shown in the preceding section that not only EMIC waves but also chorus waves are expected to be generated during large-pressure pulses. A recent study has demonstrated that the additional presence of chorus waves can actually help EMIC waves to quickly precipitate whole MeV electron populations up to the highest pitch angles [*Mourenas et al*., 2016], lending further credence to the considered precipitation mechanism.

Summers and Thorne [2003] discussed the pitch angle scattering of relativistic $E\leq1$ MeV electrons by EMIC waves. However, their interest was for magnetic storms where the region of interest was $L<6$. They found that significant scatter can only occur in high-density regions like the duskside plasmapause. Our interests here are for $L>6$ outside the plasmasphere.

4.4. Ground-Based EMIC Wave Detection

Figures 7 (top) to 7 (bottom) are the solar wind ram pressure and two dynamic spectra of the ISEE ground-based induction magnetometers, one at Athabasca, Canada (61.7° magnetic latitude; midnight: 08 UT) and the other at Moshiri, Japan (35.6° magnetic latitude; midnight: 15 UT). This is event 8 in Tables 1 and 2, an event on 27 February 2008. The wave frequencies from ~1610 UT to ~1740 UT at Athabasca were ~0.2 to 0.7 Hz. Applying the International Geomagnetic Reference Field and T02 (different) magnetospheric models, these wave frequency limits are roughly between the O^+ and He^+ gyrofrequencies at the magnetic equator [*Sakaguchi et al*., 2008]. This identifies the wave mode as EMIC waves.

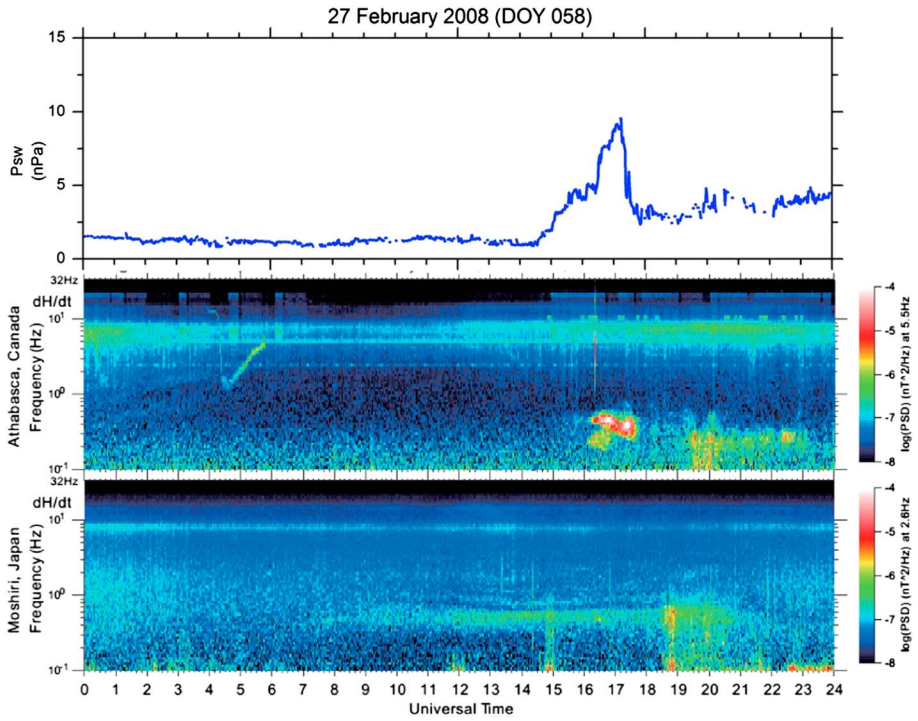

Figure 7. (top) Solar wind pressure pulse and wave data at (middle) Athabasca, Canada, at 61.7° magnetic latitude, and (bottom) Moshiri, Japan, at 35.6° magnetic latitude.

Figure 7 (top) shows the HPS density pulse. The EMIC waves at Athabasca are present and intense (up to 10^{-5} nT^2/Hz at ~0.5 Hz) where the density is highest from ~1610 to ~1740 UT (0810 to 0940 LT). There is a presence of lower amplitude EMIC waves all the way to ~2330 UT at lower frequencies.

We note that in Figure 7, the pressure pulse starts gradually from ~1430 UT to ~1730 UT. During this interval there are no EMIC waves detected at Athabasca. We suspect that with lower ram pressures, the EMIC generation would occur at higher latitudes and were undetectable at Athabasca. It was only when the magnetosphere was compressed further after ~1730 UT that proton anisotropies were high enough on the Athabasca L shell to generate waves there. There is a good correlation between the high ram pressure interval and EMIC waves at Athabasca. It is noted that no waves were detected at lower latitudes in postmidnight local times as indicated by the Moshiri data.

The ISEE magnetometer chain was started in 2005, so the coverage was available for only HPS events 6–8. The Athabasca data were not available for event 7. However, event 6 data were available, and EMIC waves were also detected during that event as well. EMIC waves were detected at 20–21 UT (12–13 LT) on 25 February 2007 (DOY 56) in the dayside sector. Thus, we can state that EMIC waves were detected on the ground whenever the Athabasca station was in the correct local time region.

4.5. The Wall of Coherent EMIC Waves

From the above numbers, relativistic electrons interacting with coherent EMIC waves in the outer zone dayside magnetosphere will be quickly scattered into the loss cone and be lost to the auroral zone atmosphere. We can conclude that if the solar wind pressure pulse generates such coherent, large-amplitude EMIC waves, the relativistic electron loss cone would be filled wherever such waves exist (see also *Meredith et al.* [2003b], *Liu et al.* [2012], and *Su et al.* [2013] for discussion of relativistic electron pitch angle scattering with incoherent EMIC waves). In general, with typical wave amplitudes, relativistic electrons can be driven into strong pitch angle diffusion even without the factor of wave coherence [*Meredith et al.*, 2003b]. However, now with EMIC wave coherence [*Remya et al.*, 2015], the pitch angle scattering rates will be orders of magnitude faster than indicated in previous quasi-linear studies, provided that trapping by coherent EMIC waves is sufficiently stable, as seems to be the case [*Artemyev et al.*, 2015].

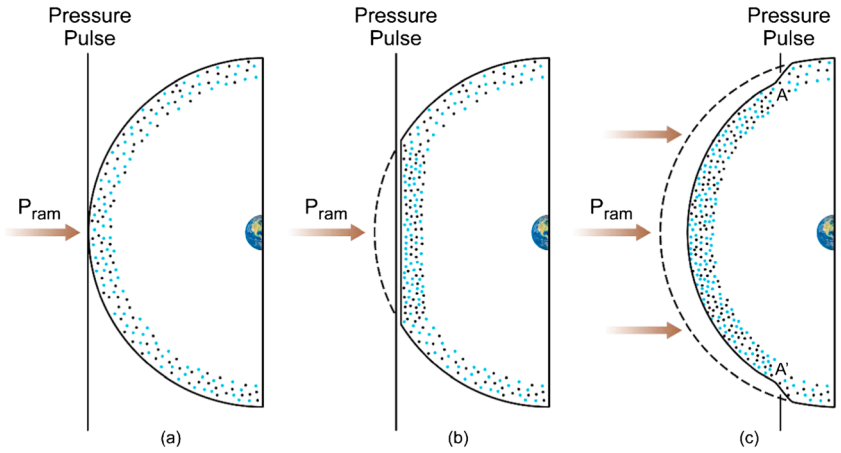

Figure 8. (a–c) Polar Orbiting Environmental Satellite. A schematic of a solar wind pressure pulse compressing the outer portion of the dayside magnetosphere. The dots represent ~10–100 keV electrons (blue) and protons (black). The particle densities and the temperatures perpendicular to the magnetic field ($T\perp$) are enhanced by the magnetospheric compression due to the solar wind HPS impingement.

Figure 8 shows a schematic illustrating the solar wind compression of the Earth's magnetosphere. The Sun is on the left (off the page), and the view is from the north pole of the Earth. The semicircle in Figure 8a represents the dayside portion of the magnetosphere. The dots indicate preexisting outer zone magnetospheric energetic ~10–100 keV electrons (blue) and ions (black). The front of the pressure pulse is indicated by the vertical line. For simplicity it is assumed that the pressure pulse originally has a planar surface oriented orthogonal to the radial direction of the solar wind flow. The magnetospheric compression starts first at the nose of the magnetosphere (Figure 8a) and then spreads to both earlier and later magnetospheric local times as the pressure pulse propagates downstream (Figures 8b and 8c). The relative magnetic compression $\Delta B/B_0$ will be greatest at the outer edge of the magnetosphere where the ambient magnetic field, B_0, is the weakest. It should be noted that although not indicated in the schematic, all regions of the magnetosphere will be compressed, even regions close to the plasmasphere ($L \sim 5$ to 6). However, the relative compression, $\Delta B/B_0$, will be the greatest near the magnetopause ($L \sim 10$) and least near the plasmapause ($L \sim 6$).

The compression of the magnetospheric magnetic field will cause betatron acceleration of both the preexisting protons and the preexisting electrons, increasing their $T_\perp$, their temperature perpendicular to B_0. This preferential heating will lead to $T_\perp/T_{||} > 1$ temperature instabilities for both the protons and electrons, causing growth of the EMIC proton cyclotron waves and the chorus electron cyclotron waves as shown in the previous subsection.

This schematic is in good agreement with the simultaneously detected EMIC and chorus waves shown in Figure 5. In that figure, both the EMIC waves and chorus were detected throughout the outer magnetosphere from L = ~10.0 to ~7.0 close to the magnetic equator.

Assuming a solar wind speed of ~700 km/s and a quiet-time magnetopause nose location of ~10 R_E, the solar wind compression from noon at the magnetopause nose to 10 and 14 magnetic local times (MLTs) (intermediate between Figures 8b and 8c) will occur in slightly less than ~1 min. EMIC waves will grow and be present in the outer region of the dayside auroral zone magnetosphere. The proton cyclotron $T_\perp/T_{||} > 1$ temperature anisotropy instability will lead to scattering of the ~10–100 keV protons and loss to the ionosphere.

Figure 9 shows a schematic of the drift orbits of ~10–100 keV protons and relativistic electrons during compressed dayside magnetospheric conditions. The view is from the Earth's North Pole with the Sun at the top of the figure (not shown). The dashed black and dashed red circles show the orbits of the ~10–100 keV protons and relativistic electrons prior to an external pressure pulse, respectively. The protons move in a clockwise motion and the relativistic electrons in an anticlockwise sense.

With an enhanced solar wind ram pressure, the magnetopause will move inward as indicated by the light blue-colored magnetopause. This compression will change the energetic charged particle drift orbits. Due to drift-shell splitting (Shabansky orbits), the protons and relativistic electrons will drift to larger L [*Roederer*

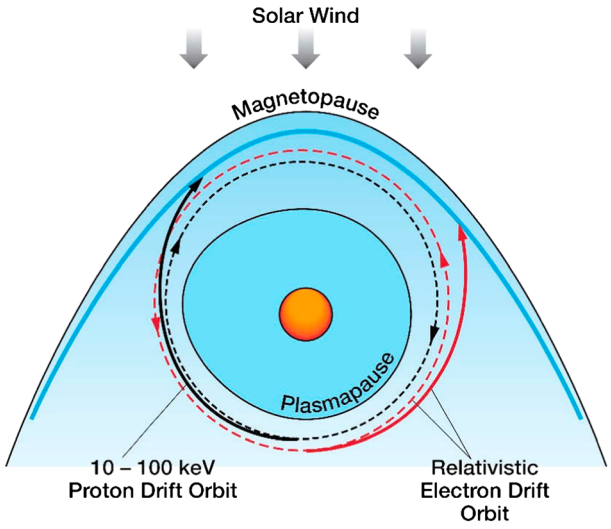

Figure 9. A schematic of the drift of energetic ~10–100 keV protons (black) and relativistic electrons (red) under both quiet (dashed lines) and compressed (solid lines) magnetospheric conditions. The magnetopause prior to the solar wind pressure pulse (quiet) is indicated in black and the new location under higher solar wind pressure (compressed) is shown in blue. The drift orbit of ~10–100 keV protons are shown in black and the drift of relativistic electrons shown in red.

and Zhang, 2014]. This is the principle for particle loss through magnetopause shadowing (for the relativistic electrons). However, now it is realized that this same solar wind pressure creates EMIC waves. If the waves are coherent, much of the protons and relativistic electrons will precipitate into the ionosphere before they reach the magnetopause.

The drift of ~1 MeV relativistic electrons around the magnetosphere is quite rapid, ~ 6–12 min [*Lew*, 1961] for a complete orbit (see the "drift echoes" for ~15 MeV electrons in *Blake et al.* [1992] and modeling in *Li et al.* [1993]). The relativistic electrons will gradient drift from the evening sector toward the dayside magnetopause, as shown in Figure 9. However, the electrons will encounter the coherent EMIC waves before reaching the magnetopause, and many will be rapidly pitch angle scattered and precipitated into the auroral region ionosphere. In our proposed scenario, relativistic electrons from $E = 0.6$ to 2.0 MeV in the outer magnetosphere (from the plasmapause at $L = 6$ to the magnetopause at $L = 10$) can be lost by the two mechanisms of pitch angle transport and convection across the magnetopause. The precipitation will start first close to the magnetopause where relativistic electrons near that region will be scattered as soon as EMIC waves grow to substantial amplitudes. Then as the pressure pulse penetrates deeper into the magnetosphere and the EMIC waves are generated there, those relativistic electrons will be scattered as well. Later as nightside electrons drift to the dayside, the relativistic electrons will encounter the EMIC wave region and parasitically interact with the waves ("parasitic" means that the particles interact with waves generated by other particles: in this case the EMIC waves are generated by energetic protons). Thus, in the overall scenario, the precipitation should first start at large L near the magnetopause and then migrate to somewhat lower latitudes (smaller L). As electrons initially in the nightside drift to the dayside and into the EMIC waves, those electrons will encounter the EMIC wave "wall" and will also be lost to the ionosphere. Thus, many of these relativistic trapped magnetospheric electrons may be lost before reaching the magnetopause.

5. Results: Energy Deposition Into the Atmosphere

5.1. The Total Energy of Relativistic Electrons in the Magnetosphere for $L > 6$

It is useful for our purposes to try to determine the total energy associated with relativistic magnetospheric electrons in the outer magnetosphere. For simplicity we will assume an energy of ~1 MeV for our calculations of the $E > 0.6$ MeV electrons. As previously mentioned, a flux decrease of 10^5 particles $cm^{-2}sr^{-1}s^{-1}$ in the $E > 0.6$ MeV energy range (~1 MeV electrons) was determined for RED events from Table 1. *Baumjohann and Treumann* [2012] have shown that the bounce time of a charged particle in a dipole magnetic field is given by $T_B = LR_E(3.7 - 1.6\sin\alpha)V_e$ where L is the L shell, α the particle pitch angle at the magnetic equator, and V_e the electron velocity. For relativistic electrons with pitch angle α at 45°, the bounce time is $T_B \sim 3.7$ s. Assuming a 2π steradian solid angle for downflowing particles and integrating over a bounce time, one gets 2.3×10^6 electrons cm^{-2} or ~3.7 ergs of relativistic particle energy per cm^2. Let us assume that the $E \sim 1$ MeV flux is to first-order constant from $L = 6$ to 10. The total equatorial area of the magnetosphere for the disc area from $L = 6$ to 10 is $\sim 8 \times 10^{19}$ cm^2. Thus, the total energy of ~1 MeV electrons in the magnetosphere is $\sim 3 \times 10^{20}$ ergs. See *Baker et al.* [1987], *Imhof and Gaines* [1993], and *Gaines et al.* [1995] for similar

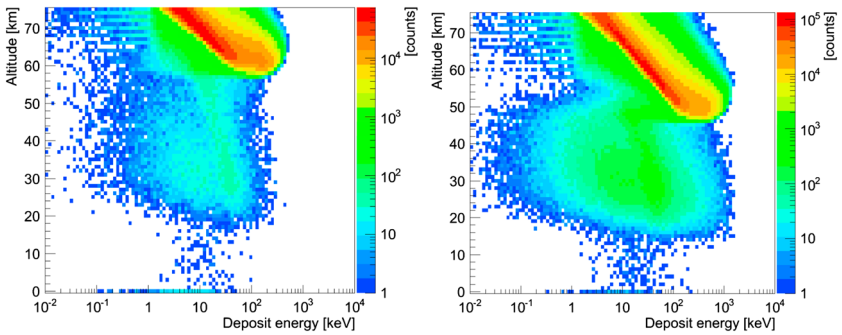

Figure 10. (left) $E > 0.6$ MeV and (right) $E > 2.0$ MeV electron precipitation energy deposition as a function of altitude. These are obtained by using the GEANT4 simulation package. The color scale is on the right of each panel.

numbers for different cases, slightly different L shell ranges, and different geomagnetic conditions. Our method of calculation is different from those of the above references.

This relativistic electron magnetospheric energy should be compared to the source energy that of the solar wind. For comparison, assuming a quiet solar wind with density ~5 cm^{-3}, a speed $V_{sw} \sim 400$ km/s and a magnetospheric circular cross section of ~ 10 R_E radius, the solar wind ram energy density impinging upon the magnetosphere would be ~3.5×10^{19} ergs/s.

5.2. Energy Deposition Into the Lower Atmosphere

Figure 10 shows the deposition of energy for $E > 0.6$ MeV electrons (left) and $E > 2.0$ MeV electrons (right) using the GEANT4 simulation package [*Agostinelli et al*., 2003] with a standard atmospheric target model [*Takada et al*., 2011]. The assumptions for the model and its application to this specific case were discussed in the section 2.1.

The energy deposition in keV is indicated by the horizontal scale, while the altitude of the energy deposition is given by the vertical scale on the left. From the figure there is a large high-energy deposition region (shown in red) that descends from > 70 km altitude to ~46 km altitude. This is due to ionization created by the energetic electrons passing through the atmosphere. The electrons stop at about 50–60 km altitude. Most of the electron energy is lost by this process.

When the relativistic electrons pass close to the atmospheric atomic or molecular nuclei, bremsstrahlung γ-rays or X-rays are produced. These energetic photons create energetic (approximately hundreds of keV) secondary electrons by Compton scattering. These secondary electrons can create further bremsstrahlung X-rays. The additional "cloud" of energy deposition in Figure 10 between ~50 km and ~18 km are due these bremsstrahlung γ-rays, X-rays, and secondary electrons. It should be noted that the > 2.0 MeV electron energy deposition reaches lower into the atmosphere than the > 0.6 MeV electrons energy deposition, as one would expect.

There is a third process for high-energy photons when $E > 1$ MeV. These γ-rays can interact with bound electrons and create e^- (electron) and e^+ (positron) pairs. These electrons and positrons can in turn create bremsstrahlung photons, and the photons (if sufficiently energetic) could create more electron-positron pairs; hence, an "electromagnetic shower" can take place. However, for our "low-energy" range of interest, 0.6 to 2.0 MeV, this process is relatively unimportant. This possibility will not be discussed further.

Figure 11 shows an intercomparison of energy deposition as a function of altitude for different relativistic electron energies (0.6, 1.0, and 2.0 MeV) at the top of the atmosphere. These particular energies were chosen as representative of relativistic electron energies measured by the NOAA GOES 8 and GOES 12 measurements shown earlier. These same energies are discussed here for particle loss calculations.

5.3. Maximum Energy Deposited Below 50 km and 30 km

We use the GEANT4 code to calculate statistically the fractional energy deposition per particle between 50 km and 30 km and below 30 km for the three energies shown in Figure 11. For the altitude range between 50 and 30 km the percent energy depositions are 0.07%, 0.13%, and 0.23% for 0.6 MeV, 1.0 MeV, and 2.0 MeV electrons,

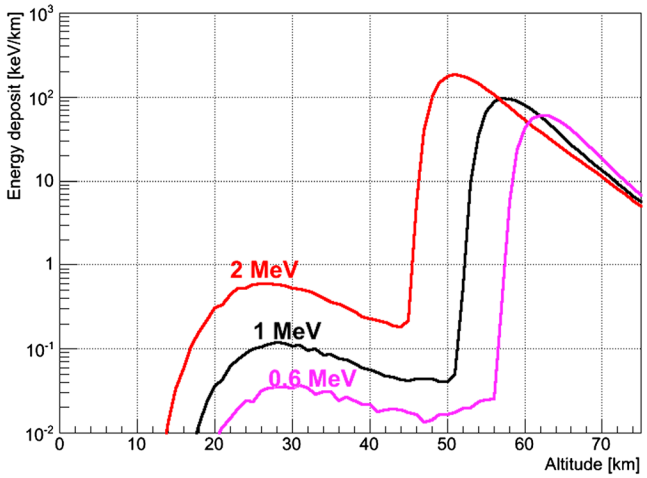

Figure 11. Energy deposition for 0.6, 1, and 2 MeV electrons entering the top of the atmosphere.

respectively. It should be noted that the percentages for the 2.0 MeV electrons are proportionally higher than those of the 0.6 and 1.0 MeV electrons, partially because the primary electrons reach ~45 km altitude.

For the fractional amount of energy that is deposited below 30 km altitude, the percentages are 0.05%, 0.1%, and 0.3%, for 0.6 MeV, 1.0 MeV, and 2.0 MeV electrons, respectively. It should be noted that for $E > 0.6$ MeV and $E > 1.0$ MeV electrons, there is slightly more energy deposited in the 50 km to 30 km range, while for the $E > 2.0$ MeV electrons, more energy is deposited below 30 km altitude than in the 50 km to 30 km range.

We now calculate the maximum energy loss to the lower atmosphere, assuming that all of the magnetospheric relativistic electrons between $L = 6$ and 10 are lost into the ionosphere/atmosphere. First consider the ~1 MeV electrons. From the previous section, it was established that there was ~3×10^{20} ergs of energy available in the magnetosphere. Thus, from the above percentages, there should be a maximum of ~4×10^{17} ergs deposited between 50 and 30 km and ~ 3.0×10^{17} ergs deposited below 30 km altitude.

It was previously mentioned in the discussion of Table 1 that the $E > 2.0$ MeV electron fluxes were about 10^3 particles $cm^{-2} sr^{-1} s^{-1}$. This flux value is 2 orders of magnitude lower than that for the $E > 0.6$ MeV electrons, so by simple scaling, the maximum energy deposition from these particles will be ~6×10^{18} ergs if all of the 2.0 MeV electrons are precipitated into the ionosphere. Following through with a similar calculation to that for the 1.0 MeV electrons, it is found that for 2.0 MeV electrons at the top of the atmosphere, a maximum of ~1.4×10^{16} ergs is deposited between 50 km and 30 km altitude and a maximum of ~1.8×10^{16} ergs is deposited below 30 km altitude.

In the above calculations we have assumed a near-maximum flux of the electrons and have also assumed all of the particles are precipitated by wave-particle interactions. Clearly, if some of the particles are lost by magnetopause shadowing, the above numbers will be lower. Also, if the relativistic electron fluxes are lower at the time of the HPS impingement onto the magnetosphere, the precipitated energies will be lower as well. These calculations of maximum energy loss to the atmosphere were done to aid others working on climate change models. The numbers are order of magnitude estimates, which should be sufficient for such studies.

6. Summary

6.1. Summary of Results

Clear examples of $E > 0.6$ MeV and $E > 2.0$ MeV relativistic electron flux dropouts (REDs) were shown (Figures 2 and 3). The properties of eight events during SC23 were reviewed in detail (Tables 1 and 2). One hundred percent of the RED event onsets were empirically associated with the impingement of high solar wind plasma density events, called heliospheric plasma sheets (HPSs), onto the magnetosphere. The HPS events are high-density regions that are physically located adjacent to the heliospheric current sheets (HCSs). HCSs are regions of interplanetary magnetic field polarity reversals (neutral sheets). Both HPSs and HCSs exist in the slow solar wind. These HPSs precede CIR and HSS encounters with the Earth because the HSSs "push" the former toward the ecliptic plane and thus HPSs/HCSs encounter the Earth's magnetosphere prior to the HSSs. This sequence of HPS/HCS, CIR, and then HSS-proper encounter is typical of what is detected at 1 AU (see Figure 1 of the present paper).

The rise in the pressure pulse of the first event shown on day 202, 1998 (Figure 2) was quite long, ~3 h. The rise was slow and monotonic. The corresponding $E > 0.6$ MeV and $E > 2.0$ MeV electron flux dropouts were quite sharp in

comparison. The 2 orders of magnitude flux decreases occurred in ~ 1–2 h. The second event on days 56 and 57, 2007 (Figure 3) was more complex. The $E > 0.6$ MeV and $E > 2.0$ MeV electron dropouts were slow and took ~9.5 h.

The other six events analyzed in this study had temporal characteristics similar to that of the Figure 2 RED event. The majority of the events (1–3, 6, and 7) had flux dropouts occurring in ~ 1 h. From all eight events, a typical flux decrease of $\sim 10^5$ electrons $cm^{-2}\,s^{-1}\,sr^{-1}$ for $E > 0.6$ MeV and $\sim 10^3$ electrons $cm^{-2}\,s^{-1}\,sr^{-1}$ for $E > 2.0$ MeV were obtained.

The predropout electron flux spectra were shown and were fit by a $J = 2 \times 10^4\, E^{-4.4}$ $cm^{-2}\,s^{-1}\,sr^{-1}$ power law, where E is the particle energy in MeV. The spectrum is very steep; e.g., there are very few electrons present at larger energies assuming that this power law holds at higher energies.

The GEANT4 simulation code was applied to a standard atmosphere to identify the fractional amount of energy deposition to the atmosphere as a function of electron energy. The percentage amount of energy deposited between 50 km and 30 km is 0.07%, 0.13%, and 0.23% for 0.6 MeV, 1.0 MeV, and 2.0 MeV electrons, respectively. For altitudes below 30 km, the percent energy deposition is 0.05%, 0.1%, and 0.3% for the same respective energy ranges. The cascade shower, particularly the electron-nucleus interaction and concomitant bremsstrahlung γ-ray and X-ray production, leads to the deep penetration of energy into the lower atmosphere.

A simple calculation showed that up to $\sim 4 \times 10^{17}$ ergs should be deposited into the atmosphere between 50 and 30 km altitude and up to $\sim 3 \times 10^{17}$ ergs should be deposited into the atmosphere at altitudes less than 30 km, if all of the relativistic electrons were lost by wave-particle interactions. Because the flux of the $E > 0.6$ MeV (read ~1.0 MeV) electrons are so much higher than the $E > 2.0$ MeV electrons, it is only the $E \sim 1.0$ MeV electrons that are of primary importance for energy deposition.

6.2. Summary of Model

The solar wind pressure pulses create the strong dayside magnetic field magnitude gradients which causes both relativistic electron drift-shell splitting and particle drifts toward the dayside magnetopause and also simultaneously create the betatron acceleration of preexisting ~10–100 keV protons (by conservation of the particles' first adiabatic invariants). For the latter mechanism, once the energetic protons are energized selectively in their perpendicular (to B_0) energy, the ion temperature anisotropy instability takes place with concomitant EMIC wave generation. It was shown by example that the EMIC waves are coherent and the electrons will be pitch angle transported by ~23° in a single 4.1 ms interaction in the example shown. The pitch angle diffusion time was shown to be of the order of 53 ms. This new finding indicates that the relativistic electrons could have a filled loss cone as they gradient drift toward the magnetopause.

It should be noted that since the majority of the relativistic electrons in the magnetosphere are outside the dayside compression region when the initiation of the compression starts, the particles must drift through the EMIC wave field on their drift orbits to the magnetopause. They will have to "run the EMIC wave gauntlet," so to speak. It is not certain how many electrons will reach the magnetopause, but the pitch angle transport times indicate that the majority of the particles will be precipitated as they go through the EMIC wave field. Detailed modeling is needed to identify what the percentage is. The reader should note that our present hypothesis includes both wave-particle interaction losses and the particle gradient drifts which lead to the magnetopause shadowing.

There are other interplanetary pressure pulses that are effective in causing relativistic electron losses. One example previously discussed was fast-forward shock compression of the magnetosphere [*Zhou and Tsurutani*, 1999; *Tsurutani et al*., 2001] leading to tailward propagating auroras. Relativistic electron precipitation should be found in those auroras as well. One such example has been shown by *Miyoshi et al*. [2008].

7. Discussion

7.1. Can the Energy Deposited in the Mesosphere Somewhere Between 50 and ~80 km Altitude Be Important? Could the Heating be Associated With Driving Planetary or Atmospheric Gravity Waves?

Figures 10 and 11 indicate that the maximum energy deposition of ~1 MeV electrons occurs at ~ 60 km altitude. This is due to the particle having the greatest $-dE/dx$ rate when the particle velocity and energy is the

lowest, near the end of the particle's range. In the above, dE is the differential energy, and dx is the amount of distance traveled. For simplicity, we take a 100 km × 100 km × 5 km volume. With a N_2 number density of ~6.7×10^{15} molecules cm^{-3}, one gets 3.3×10^{35} molecules in the volume. The relativistic electron energy deposited in this region is the majority of the energy, so an energy number like 3×10^{20} ergs can be used. This corresponds to ~9×10^{-16} ergs/molecule or +6 K if the energy is evenly distributed throughout the volume. Clearly, "hot spots" will give substantially higher temperatures, and this might be a source to directly drive the atmospheric waves. Detailed modeling will be needed to test this idea.

7.2. NO_x Production and Possible Ozone Depletion

The precipitation of energetic electrons into the atmosphere and the subsequent electron/photon energy cascade leading to ~10–100 keV secondary electrons will efficiently lead to the ionization and dissociation of N_2 molecules (see general discussion in *Thorne* [1980]) into N(^{2}D) and N(^{4}S), excited atomic nitrogen, and ground-state atomic nitrogen, respectively. Approximately 1.3 nitrogen atoms are produced for each electron-ion pair [*Brasseur and Nicolet*, 1973; *Nicolet*, 1975; *Rusch et al*., 1981]. The interaction of N with O_2 and O_3 will form NO, a catalytic molecule for the destruction of ozone. Other chemical reactions particularly those associated with NO can lead to the formation of N_2O, a greenhouse gas. We refer the reader to *Sinnhuber et al*. [2012] for a recent comprehensive review of energetic particle precipitation and the chemistry of the mesosphere/lower thermosphere.

The total production of electron-ion pairs in the atmosphere available for the production of NO_x and HO_x can be estimated using the well-known relation of ~35 eV expended per electron ion pair. For the 50 km to 30 km altitude range, there will be 7×10^{27} electron-ion pairs formed, and for the $<$ 30 km altitude range there will be 5×10^{27} electron-ion pairs formed.

Thorne [1977] had suggested that a modulation of stratospheric ozone will cause changes in both thermal structure and radiative damping properties of the middle atmosphere, which will in turn influence both the tropospheric energy budget and the reflection characteristics of atmospheric waves which are involved in the development of tropospheric weather systems. *Dennison et al*. [2015] using the National Institute of Water and Atmospheric Research-United Kingdom Chemistry and Aerosols coupled atmosphere-ocean chemistry-climate model have examined the influence of ozone depletion and recovery on the Southern Annular Mode (SAM) and have found that "depletion leads to an increased frequency of extreme anomalies and increased persistence of the SAM in the stratosphere as well as stronger, more persistent stratosphere-troposphere coupling." *Keeble et al*. [2014] using a fully coupled UM-UKCA chemistry climate model have noted that a polar stratospheric ozone loss leads to an acceleration of the polar vortex with a delay in its breakdown by ~2 weeks. There is increased wave activity entering the stratosphere with subsequent wave breaking at higher altitudes.

It should be mentioned that the latitude range of the predicted relativistic electron precipitation should occur over a region of partly sunlit atmosphere and partly dark atmosphere in spring. *Thorne* [1980] has pointed out that during polar night, neither the ozone photoproduction nor the catalytic destruction mechanism can operate. Thus, the dark portions of the atmosphere will be unusually devoid of ozone and the neighboring sunlit portion of the atmosphere recovering due to photoproduction. This temporal variation needs to be examined further.

7.3. Can the Destruction of Ozone in the Stratosphere Be Important?

This is another result of the relativistic electron precipitation. It is also important to note that the general region of precipitation $L = 6$ to 10 corresponds to magnetic latitudes of ~65° to 72° (assuming a dipole magnetic field). Assuming that this corresponds roughly to geographic latitudes for simplicity, at Northern Hemisphere winter, half of this region will be in sunlight and half will be in darkness. Without a reduction of ozone in the stratosphere, the solar radiation will be absorbed at the tropopause. Could the additional heating lead to instability of this structure?

8. Discussion of Related Observations and Models to HCS Crossings, HSSs, and REDs

8.1. HCS Crossings and Atmospheric Winds

Wilcox et al. [1973] have reported a relationship between interplanetary heliospheric current sheet (HCS) crossings and atmospheric winds. They studied the average area of high positive vorticity centers

(low-pressure troughs) observed during Northern Hemispheric winters at the ~300 mbar level. They showed by statistics that the average area of high vorticity decreased near the time of HCS crossings. We have shown in this paper that it is the HPSs adjacent to the HCS crossings that can have significant effects to magnetospheric relativistic electrons. Our hypothesis is that it is the REDs associated with the HPS crossings and not the HCS crossings that are causing the Wilcox et al. effect.

8.2. REDs and HCS Crossings and HSSs

Borovsky and Denton [2009] have identified RED occurrence in a superposed epoch study. They find that the relativistic electron flux dropouts "occur after the IMF HCS reversal prior to the passage of corotating interaction region (CIR) stream interfaces in the HSSs." They speculated that injections of a superdense ion plasmasheet into the nightside magnetosphere, the formation of a plasmaspheric plume/tail, and EMIC wave generation as energetic protons drift into the high-density plume. Their hypothesis is that the relativistic electrons are lost by pitch angle scattering with the EMIC waves. The *Borovsky and Denton* [2009] study use low time resolution data and averaged events for their superposed epoch analyses. We suggest that it is HPS ram pressure pulses which occur in the slow solar wind which generate the coherent EMIC waves and cause the REDs. A plasma plume and particle injections are not necessary in our model.

Meredith et al. [2011] have used the NOAA Polar Orbiting Environmental Satellite (POES) spacecraft data to study REDs during 42 HSS-driven storm events. They find that trapped and precipitation relativistic electrons with $E > 1$ MeV drop out following (CIR) storm onsets. Again, this was a low time resolution study. We suggest that it is not CIR storms but HPS pressure pulse events that cause the REDs.

8.3. HCS Crossings, Interplanetary Relativistic Electrons, and the Global Electric Circuit

Tinsley and Deen [1991] have proposed that an induced change in the current density of the global electric circuit could lead to climate change. The above paper was related to ionization effects from cosmic rays in the middle stratosphere. Later *Tinsley et al*. [1994] suggested that relativistic electrons could also cause the same effect. They stated the following: "This (HCS) current sheet often acts as a boundary between high-speed streams in the solar wind, and the fluxes of relativistic electrons are found to increase following the passage of high-speed streams… precipitation of such relativistic electrons into the atmosphere produces bremsstrahlung which changes the atmospheric conductivity at least down to the middle stratosphere. It is suggestive that the minimum in such precipitation occurs at the time of the minimum in air-earth current density." In the present paper we find no such interplanetary relativistic electrons, but we do show the disappearance (and suggested precipitation) of relativistic magnetospheric electrons.

Lam et al. [2013] have proposed an interplanetary magnetic field B_y fluctuation effect (HCS crossings) as a mechanism of Sun-weather coupling. They have shown that the difference between the mean surface pressures during times of high positive and high negative IMF B_y possesses a statistically significant midlatitude wave structure similar to atmospheric Rossby waves. For a review of different space weather-climate changing mechanisms, we refer the reader to *Lam and Tinsley* [2015].

8.4. HCS Crossings, CIRs, and Lightning Flashes

Owens et al. [2015] have noted a correlation between lightning flashes over the UK and the passage of interplanetary HCSs. They speculate that it may be the CIRs in the stream-stream interaction regions (please refer to Figure 1) that are causing the "compression/amplification of the heliospheric magnetic field (HMF)."

8.5. Sudden Stratospheric Warmings (SSWs)

A Sudden Stratospheric Warming (SSW) event was originally called a "Berlin Phenomenon" when R. Scherhag discovered a sudden increase in the radiosonde 10 mbar temperature over Berlin on 30 January 1952 [*Scherhag*, 1952]. However, it was later realized that this local phenomena was related to weather over most of the Northern Hemisphere [*Scherhag*, 1960] and the name was changed. *Palmer* [1959] *and Scherhag* [1960] related SSWs to solar events (with delays), but *Reed et al*. [1963] and *Schoeberl* [1978] argued that it was atmospheric gravity waves that were the cause. SSWs were later described as "an abrupt temperature warming of the polar stratosphere associated with the breakdown of the cold polar vortex" [World Meteorological

Organization, 1978; see also *Harada et al*., 2010]. One should ask the important question: "what is the energy source for SSWs"?

9. Conclusions

The overall scenario of our model is that high-density HPSs impact the magnetosphere compressing both the magnetosphere and the preexisting ~10–100 keV energetic particles within it. This pressure pulse impaction causes two things. It leads to the generation of coherent EMIC waves in the dayside outer magnetosphere and also causes the rapid gradient drift of relativistic electrons toward the dayside magnetopause. The relativistic electrons have to run the gauntlet through the EMIC waves, and many can be pitch angle scattered and lost to the atmosphere before they reach the magnetopause. This is suggested as the cause of the REDs in our model. Other solar wind structures like CIRs can also compress the magnetosphere. However, from Figure 1 it is noted that HPSs which occur in the slow solar wind impact the magnetosphere first and deplete the magnetosphere of the relativistic electrons. By the time the CIRs reach the magnetosphere, the relativistic electrons have already been lost. It is not until the HSS/HILDCAA interval that the relativistic electrons repopulate the magnetosphere [*Hajra et al*., 2015a].

In this present paper, we have provided a possible energy source as a trigger for the *Wilcox et al*. [1973] HCS-stratospheric wind effect. At the same time we have provided the relativistic electron source for the *Tinsley et al*. [1994] global circuit alteration mechanism. Both of the phenomena have important consequences for atmospheric weather.

The energy is the stored kinetic energy of the relativistic ~ 1 MeV electrons orbiting in the outer magnetosphere between $L = 6$ and 10. What is particularly significant about our proposed mechanism is that relativistic electron precipitation is able to cause the deposition of substantial energy in the mesosphere (~100 km to ~50 km altitude) and also in the stratosphere (~50 km to ~10 km). In contrast, the stratospheric energy deposition does not occur with solar flare protons with ~1 to 100 MeV kinetic energies precipitating into the atmosphere. Energetic protons lose their energy by ionization of the atmospheric atoms and molecules. Relativistic electrons are more effective for low-altitude energy deposition because when they pass close to atomic and molecular nuclei, they generate bremsstrahlung γ-rays and X-rays which have much greater penetration power than do charged particles.

We have shown that there is substantial energy deposition (up to 3×10^{20} ergs) that can occur at auroral zone ($L = 6$ to 10) latitudes. These L shells correspond to ~65° to 72° magnetic latitudes assuming a dipole magnetic field.

The majority of this energy is deposited in the lower mesosphere due to particle ionization losses. This concentrated energy loss far exceeds that deposited by solar flare protons (the protons are very energetic, but the flux is considerably lower) or galactic cosmic rays [*Thorne*, 1977; *Baker et al*., 1987]. Occasionally, there are solar flare relativistic electron events [*Pesnell et al*., 1999], but these fluxes are lower and will be lost over a much greater surface area of the Earth's ionosphere.

Thus, our current mechanism may be a means of acting as a catalyst for the generation of planetary waves and atmospheric gravity waves at mesospheric and stratospheric heights. It is known that atmospheric waves are associated with SSWs [*Harada et al*., 2010; *Oberheide et al*., 2015]. Influence of the upper atmosphere on the troposphere is thought to occur by altering the reflection characteristics of long-wavelength waves that are involved in the development of tropospheric weather systems [*Thorne*, 1977; *Geller and Alpert*, 1980]. So the precipitation of relativistic electrons in a relatively confined region of the atmosphere might be an important feature influencing the atmosphere that should be studied further.

Another possible mechanism is the NO production throughout the stratosphere by the cascade of γ-rays, X-rays, and secondary electrons. The NO molecules will catalytically destroy ozone throughout the stratosphere, with the result of a lack of solar UV absorption in this region, leading to temperature decreases. This in turn may affect the stability of atmospheric temperature profile, perhaps leading to an instability (upwelling) of the tropopause.

Further observations in X-rays and γ-rays and relativistic electrons are needed to determine if some of the conjectures of our scenario are borne out or not. Modeling of various parts of the atmosphere with the specified energy inputs also may give further insights as to atmospheric dynamics.

Appendix A

Table A1. EMIC Wave Search for the Eight Pressure Pulse Events Identified in Tables 1 and 2[a]

		Cluster		THEMIS	
No.	Events DOY	Position (GSE Coordinates)	Waves	Position (GSE Coordinates)	Waves
1	1995-150	NA	NA	NA	NA
2	1998-202	NA	NA	NA	NA
3	2000-027	NA	NA	NA	NA
4	2000-052	NA	NA	NA	NA
5	2003-258	On night side [−17.8, 4.8, −5.2] R_E at 16:32UT (~23:24 LT)	No EMIC waves	NA	NA
6	2007-056	In outer magnetosphere after 2200 till 2359 UT	No EMIC waves observed	NA	NA
		[9.6, −3.6, −11.0] R_E at 2200 UT (~12:35 LT)	High-frequency waves are observed with $f = 3–5 \times f_{cp}$		
7	2007-243	Night side [−16.7, −4.9, −2.9] R_E at 1343 UT (~01:16 LT)	No EMIC waves	Entered magnetosheath at ~13:30 UT [7.6, −8.7 1.2] R_E at 1340 UT (~08:43 LT)	No EMIC waves observed
8	2008-058	Within ~2 R_E of Earth ~ [2.8, −4.7, −7.2] R_E at 1407 UT (~08:47 LT)	NA	[−1.0, −2.5, −0.3] R_E at 1400 UT (~05:02 LT) high-resolution data are not available	NA

[a]The four Cluster spacecraft and the two THEMIS spacecraft were used in the search. The columns are as follows, from left to right: the event number, the year and day of the event, the location of Cluster, wave/no wave detection, the location of THEMIS, and wave/no wave detection.

Acknowledgments

We wish to thank J. Bortnik for useful discussions on magnetopause shadowing and S. Yagitani for searching for Geotail locations. Portions of the research were conducted at the Jet Propulsion Laboratory, California Institute of Technology, under contract with NASA. B.T.T. would like to thank M. Honchell of the JPL Library for finding many of the references listed in this paper. The work of R.H. is financially supported by Fundação de Amparo à Pesquisa do Estado de São Paulo (FAPESP) through postdoctoral research fellowship at INPE. G.S.L. thanks the National Academy of Sciences, India, for support under the NASI-Senior Scientist Platinum Jubilee Fellowship Scheme. Work done by J.U.K. was supported by the National Science Foundation through Independent Research and Development for staff. E.E. would like to thank to the Brazilian CNPq (302583/2015-7) agency for financial support. B. R. would like to thank Academia Sinica, Taiwan, for providing financial support through a postdoctoral research fellowship. Observations at Athabasca and Moshiri are supported by JSPS KAKENHI (15H05815 and 16H06286). Solar wind/interplanetary data at 1 min time resolution were obtained from the OMNI website (http://omniweb.gsfc.nasa.gov/). The *AE* (1 min), *SYM-H* (1 min) and *Dst* (1 h) geomagnetic indices were obtained from the World Data Center for Geomagnetism, Kyoto, Japan (http://wdc.kugi.kyoto-u.ac.jp).

References

Agostinelli, S., et al. (2003), GEANT4—A simulation toolkit, *Nucl. Instr. Meth. in Phys. Res. Sect. A*, *506*, 250, doi:10.1016/S0168-9002(03)01368-8.

Akasofu, S.-I. (1964), The development of the auroral substorm, *Planet Space Sci.*, *12*, 273, doi:10.1016/0032-0633(64)90151-5.

Albert, J. M. (2014), Radiation diffusion simulations of the 20 September 2007 radiation belt dropout, *Ann. Geophys.*, *32*, 925, doi:10.5194/angeo-32-925-2014.

Alfvén, H. (1977), Electric currents in cosmic plasmas, *Rev. Geophys. Space Phys.*, *15*, 271, doi:10.1029/RG015i003p00271.

Anderson, B. J., and D. C. Hamilton (1993), Electromagnetic ion cyclotron waves stimulated by modest magnetospheric compressions, *J. Geophys. Res.*, *98*, 11,369, doi:10.1029/93JA00605.

Angelopoulos, V., et al. (2008), First results from the THEMIS mission, *Space Sci. Rev.*, *141*(1), 453, doi:10.1007/s11214-008-9378-4.

Artamonov, A. A., A. L. Mishev, and I. G. Usoskin (2016), Atmospheric ionization induced by precipitating electrons: Comparison of CRAC:EPII model with parametrization model, preprint *Astro-ph.EP*, arXiv:1601.05910v1.

Artemyev, A. V., A. A. Vasiliev, D. Mourenas, O. V. Agapitov, V. Krasnoselskikh, D. Boscher, and G. Rolland (2014), Fast transport of resonant electrons in phase space due to nonlinear trapping by whistler waves, *Geophys. Res. Lett.*, *41*, 5727–5733, doi:10.1002/2014GL061380.

Artemyev, A. V., D. Mourenas, O. V. Agapitov, D. L. Vainchtein, F. S. Mozer, and V. Krasnoselskikh (2015), Stability of relativistic electron trapping by strong whistler or electromagnetic ion cyclotron waves, *Phys. Plasma*, *22*, 082901, doi:10.1063/1.497774.

Auster, H. U., et al. (2008), The THEMIS fluxgate magnetometer, *Space Sci. Rev.*, *141*(1), 235, doi:10.1007/s11214-008-9365-9.

Baker, D. N., J. B. Blake, D. J. Gorney, P. R. Higbie, R. W. Klebesadel, and J. H. King (1987), Highly relativistic magnetospheric electrons: A role in coupling to the middle atmosphere?, *Geophys. Res. Lett.*, *14*, 1027, doi:10.1029/GL014i010p01027.

Baker, D. N., J. B. Blake, L. B. Callis, J. R. Cummings, D. Hovestadt, S. Kanekal, B. Klecker, R. A. Mewaldt, and R. D. Zwickl (1994), Relativistic electron acceleration and decay time scales in the inner and outer radiation belts: SAMPEX, *Geophys. Res. Lett.*, *21*, 409, doi:10.1029/93GL03532.

Balogh, A., et al. (2001), The Cluster Magnetic Field Investigation: Overview of in-flight performance and initial results, *Ann. Geophys.*, *19*, 1207, doi:10.5194/angeo-19-1207-2001.

Baumjohann, W., and R. A. Treumann (2012), *Basic Space Plasma Physics*, Imperial College Press, London.

Belcher, J. W., and L. Davis Jr. (1971), Large-amplitude Alfvén waves in the interplanetary medium: 2, *J. Geophys. Res.*, *76*, 3524, doi:10.1029/JA076i016p03534.

Bellan, P. M. (2013), Pitch angle scattering of an energetic magnetized particle by a circularly polarized electromagnetic wave, *Phys. Plasma*, *20*, 042117, doi:10.1063/1.4801055.

Blake, J. B., W. A. Kolasinski, R. W. Fillius, and E. G. Mullen (1992), Injection of electrons and protons with energies of tens of MeV into $L < 3$ on March 24, 1991, *Geophys. Res. Lett.*, *19*, 821, doi:10.1029/92GL00624.

Borovsky, J. E., and M. H. Denton (2009), Relativistic-electron dropouts and recovery: A superposed epoch study of the magnetosphere and the solar wind, *J. Geophys. Res.*, *114*, A02201, doi:10.1029/2008JA013128.

Bortnik, J., R. M. Thorne, T. P. O'Brien, J. C. Green, R. J. Strangeway, Y. Y. Shprits, and D. N. Baker (2006), Observation of two distinct, rapid loss mechanisms during the 20 November 2003 radiation belt dropout event, *J. Geophys. Res.*, *111*, A12216, doi:10.1029/2006JA011802.

Boyd, A. J., H. E. Spence, S. G. Claudepierre, J. F. Fennell, J. B. Blake, D. N. Baker, G. D. Reeves, and D. L. Turner (2014), Quantifying the radiation belt seed population in the March 17, 2013 electron acceleration event, *Geophys. Res. Lett.*, *41*, 2275–2281, doi:10.1002/2014GL050626.

Brasseur, G., and M. Nicolet (1973), Chemospheric processes of nitric oxide in the mesosphere and stratosphere, *Planet Space Sci.*, *21*, 939, doi:10.1016/0032-0633(73)90141-4.

The integrated fluxes of relativistic > 0.6 and > 2.0 MeV electrons at geosynchronous orbit (L = 6.6) were taken by GOES 8 and GOES 12 satellite particle instrumentation. The data website is http://www.ngdc.noaa.gov/stp/satellite/goes/dataaccess.html. The five vector/s Cluster magnetometer data were obtained from the Cluster Science Archive (CSA). The four vector/s magnetometer data from THEMIS was obtained from the SPDF CDAWeb. For the study of EMIC wave occurrence on the ground, we use data from the Nagoya University Institute for Space-Earth Environmental Research (ISEE) magnetometer network (http://stdb2.isee.nagoya-u.ac.jp/magne/index.html). We wish to thank the three reviewers for their extremely helpful and constructive comments. These helped improve our paper greatly.

Brautigam, D. H., and J. M. Albert (2000), Radial diffusion analysis of outer radiation belt electrons during the October 9, 1990, magnetic storm, *J. Geophys. Res.*, *105*, 291, doi:10.1029/1999JA900344.

Brice, N. (1964), Fundamentals of very low frequency emission generation mechanisms, *J. Geophys. Res.*, *69*, 4515, doi:10.1029/JZ069i021p04515.

Clilverd, M. A., C. J. Rodger, and T. Ulich (2006), The importance of atmospheric precipitation in storm-time relativistic electron flux drop outs, *Geophys. Res. Lett.*, *33*, L01102, doi:10.1029/2005GL024661.

Clilverd, M. A., C. J. Rodger, M. Andersson, P. T. Verronen, and A. Seppälä (2016), Linkage between the radiation belts, polar atmosphere and climate: Electron precipitation through wave particle interactions, in *Waves, Particles and Storms in Geospace*, edited by. I. Mann et al., Oxford Univ. Press, Oxford, U. K.

Cornwall, J. M. (1965), Cyclotron instabilities and electromagnetic emissions in the ultra low frequency and low frequency ranges, *J. Geophys. Res.*, *70*, 61, doi:10.1029/JG070i001p00061.

Craven, J. D., L. A. Frank, C. T. Russell, E. J. Smith, and R. P. Lepping (1986), Global auroral responses to magnetospheric compression by shocks in the solar wind: Two case studies, in *Solar Wind-Magnetosphere Coupling*, edited by Y. Kamide and J. A. Slavin, 367 pp., Terra Sci., Tokyo.

Davis, T. N., and M. Sugiura (1966), Auroral electrojet activity index *AE* and its universal time variations, *J. Geophys. Res.*, *71*, 785, doi:10.1029/JZ071i003p00785.

DeForest, S. E., and C. E. McIlwain (1971), Plasma clouds in the magnetosphere, *J. Geophys. Res.*, *76*, 3587, doi:10.1029/JA076i016p03587.

Dennison, F. W., A. J. McDonald, and O. Morgenstern (2015), The effect of ozone depletion on the Southern Annular Mode and stratosphere-troposphere coupling, *J. Geophys. Res. Atmos.*, *120*, 6305–6312, doi:10.1002/2014JD023009.

Dessler, A. J., and R. Karplus (1961), Some effects of diamagnetic ring currents on Van Allen radiation, *J. Geophys. Res.*, *66*, 2289, doi:10.1029/JZ066i008p02289.

Dessler, A. J., and E. N. Parker (1959), Hydromagnetic theory of magnetic storms, *J. Geophys. Res.*, *64*, 2239, doi:10.1029/JZ064i012p02239.

Dimitrakoudis, S., I. R. Mann, G. Balasis, C. Papadimitriou, A. Anastasiadis, and I. A. Daglis (2015), *Geophys. Res. Lett.*, *42*, 5711–5718, doi:10.1002/2015GL064707.

Engebretson, M. J., W. K. Peterson, J. L. Posch, M. R. Klatt, B. J. Anderson, C. T. Russell, H. J. Singer, R. L. Arnoldy, and H. Fukunishi (2002), Observations of two types of Pc 1-2 pulsations in the outer dayside magnetosphere, *J. Geophys. Res.*, *107*(A12), 1415, doi:10.1029/2001JA00198.

Escoubet, C. P., M. Fehringer, and M. Goldstein (2001), Introduction the Cluster mission, *Ann. Geophys.*, *19*, 1197, doi:10.5194/angeo-19-1197-2001.

Frank, L., J. A. Van Allen, W. A. Whelpley, and J. D. Craven (1963), Absolute intensities of geomagnetically trapped particles with Explorer 14, *J. Geophys. Res.*, *68*, 1963.

Freeman, J. W., Jr. (1964), The morphology of the electron distribution in the outer radiation zone and near the magnetospheric boundary as observed by Explorer 12, *J. Geophys. Res.*, *69*, 1691, doi:10.1029/JZ069i009p01691.

Friedel, R. H. W., G. D. Reeves, and T. Obara (2002), Relativistic electron dynamics in the inner magnetosphere—A review, *J. Atmos. Sol. Terr. Phys.*, *64*, 265, doi:10.1016/S1364-6826(01)00088-8.

Gabrielse, C., V. Angelopoulos, A. Runov, and D. L. Turner (2014), Statistical characteristics of particle injections throughout the equatorial magnetotail, *J. Geophys. Res. Space Physics*, *119*, 2512–2535, doi:10.1002/2013JA019638.

Gaines, E. E., D. L. Chenette, and W. L. Imhof (1995), Relativistic electron fluxes in May 1992 and their effects on the middle atmosphere, *J. Geophys. Res.*, *100*, 1027, doi:10.1029/94JD02615.

Geller, M. A., and J. C. Alpert (1980), Planetary wave coupling between the troposphere and the middle atmosphere as a possible Sun-weather mechanism, *Am. Meteorol. Soc.*, *37*, 1198.

Gonzalez, W. D., J. A. Joselyn, Y. Kamide, H. W. Kroehl, G. Rostoker, B. T. Tsurutani, and V. M. Vasyliunas (1994), What is geomagnetic storm?, *J. Geophys. Res.*, *99*, 5771, doi:10.1029/93JA02867.

Guarnieri, F. L. (2006), The nature of auroras during High-Intensity Long-Duration and Continuous AE Activity (HILDCAA) events: 1998 to 2001, in *Recurrent Magnetic Storms, Corotating Solar Wind Streams*, *Geophys. Monogr. Ser.*, vol. 167, edited by B. Tsurutani et al., 235 pp., AGU, Washington, D. C.

Gurnett, D. A., et al. (1994), The Cassini radio and plasma wave investigation, *Space Sci. Rev.*, *114*, 395, doi:10.1007/s11214-004-1434-0.

Hajra, R., E. Echer, B. T. Tsurutani, and W. D. Gonzalez (2013), Solar cycle dependence of High-Intensity Long-Duration Continuous AE Activity (HILDCAA) events, relativistic electron predictors?, *J. Geophys. Res. Space Physics*, *118*, 5626–5638, doi:10.1002/jgra.50530.

Hajra, R., B. T. Tsurutani, E. Echer, and W. D. Gonzalez (2014a), Relativistic electron acceleration during High-Intensity, Long-Duration, Continuous AE Activity (HILDCAA) events: Solar cycle phase dependences, *Geophys. Res. Lett.*, *41*, 1876–1881, doi:10.1002/2014GL059383.

Hajra, R., E. Echer, B. T. Tsurutani, and W. D. Gonzalez (2014b), Superposed epoch analyses of HILDCAAs and their interplanetary drivers: Solar cycle and seasonal dependences, *J. Atmos. Sol. Terr. Phys.*, *121*, 24, doi:10.1016/j.jastp.2014.09.012.

Hajra, R., B. T. Tsurutani, E. Echer, W. D. Gonzalez, and O. Santolik (2015a), Relativistic (E > 0.6, > 2.0 and > 4.0 MeV) electron acceleration at geosynchronous orbit during High-Intensity Long-Duration Continuous AE Activity (HILDCAA) events, *Astrophys. J.*, *799*, 39, doi:10.1088/0004-637X/799/1.39.

Hajra, R., B. T. Tsurutani, E. Echer, W. D. Gonzalez, C. G. Brum, L. E. A. Viera, and O. Santolik (2015b), Relativistic electron acceleration during HILDCAA events: Are precursor CIR magnetic storms important?, *Earth Planets Space*, *67*, 109, doi:10.1186/s40623-015-0280.5.

Harada, Y., A. Goto, H. Hasegawa, N. Fujikawa, H. Naoe, and T. Hirooka (2010), A major stratospheric sudden warming event in January, 2009, *J. Atmos. Sci.*, *67*, 2052, doi:10.1175/2009JAS3320.1.

Horne, R. B., and R. M. Thorne (1998), Potential waves for relativistic electron scattering and stochastic acceleration during magnetic storms, *Geophys. Res. Lett.*, *25*, 3011, doi:10.1029/98GL01002.

Horne, R. B., M. M. Lam, and J. C. Green (2009), Energetic electron precipitation from the outer radiation belt during geomagnetic storms, *Geophys. Res. Lett*, *36*, L19104, doi:10.1029/2009GL040236.

Hudson, M. K., D. N. Baker, J. Goldstein, B. T. Kress, J. Paral, F. R. Toffoletto, and M. Wiltberger (2014), Simulated magnetopause losses and Van Allen Probe flux dropouts, *Geophys. Res. Lett.*, *41*, 1113–1118, doi:10.1002/2014GL059222.

Hundhausen, A. J. (1977), An interplanetary view of coronal holes, in *Coronal Holes and High Speed Wind Streams*, edited by J. B. Zirker, Univ. Colo. Press, Boulder.

Imhof, W. I., and E. E. Gaines (1993), Inputs to the atmosphere from relativistic electrons, *J. Geophys. Res.*, *98*, 13,575, doi:10.1029/93JA01149.

Inan, U. S., T. F. Bell, and R. A. Helliwell (1978), Nonlinear pitch angle scattering of energetic electrons by coherent VLF waves in the magnetosphere, *J. Geophys. Res.*, *83*, 3235, doi:10.1029/JA083iA07p03235.

Iyemori, T. (1990), Storm-time magnetospheric currents inferred from mid-latitutde geomagnetic field variations, *J. Geomagn. Geoelectr.*, *42*, 1249, doi:10.5636/jgg.42.1249.

Jordanova, V. K., J. Albert, and Y. Miyoshi (2008), Relativistic electron precipitation by EMIC waves from self-consistent global simulations, *J. Geophys. Res.*, *113*, A00A10, doi:10.1029/2008JA013239.
Kasahara, Y., Y. Miyoshi, Y. Omura, O. P. Verkhoglyadova, I. Nagano, I. Kimura, and B. T. Tsurutani (2009), Simultaneous satellite observations of VLF chorus, hot and relativistic electrons in a magnetic storm "recovery" phase, *Geophys. Res. Lett.*, *36*, L01106, doi:10.1029/2008GL036454.
Keeble, J., P. Braesicke, N. L. Abraham, H. K. Roscoe, and J. A. Pyle (2014), The impact of polar stratospheric ozone loss on Southern Hemisphere stratospheric circulation and climate, *Atmos. Chem. Phys.*, *14*, 13,705, doi:10.5194/acp-14-13705-2014.
Kellogg, P. J. (1959), Van Allen radiation of solar origin, *Nature*, *183*, 1295, doi:10.1038/1831295a0.
Kennel, C. F., and H. E. Petschek (1966), Limit on stable trapped particle fluxes, *J. Geophys. Res.*, *71*, 1, doi:10.1029/JZ071i001p00001.
Kersten, T., R. B. Horne, S. A. Glauert, N. P. Meredith, B. J. Fraser, and R. S. Grew (2014), Electron losses from the radiation belts caused by EMIC waves, *J. Geophys. Res. Space Physics*, *119*, 8820–8837, doi:10.1002/2014JA020366.
Kim, H.-J., and A. A. Chan (1997), Fully adiabatic changes in storm time relativistic electron fluxes, *J. Geophys. Res.*, *102*, 22,107, doi:10.1029/97JA01814.
Kim, K.-C., D.-Y. Lee, H.-J. Kim, L. R. Lyons, E. S. Lee, M. K. Ozturk, and C. R. Choi (2008), Numerical calculations of relativistic electron drift loss effect, *J. Geophys. Res.*, *113*, A09212, doi:10.1029/2007HA013011.
Kim, K.-C., D.-Y. Lee, H.-J. Kim, E. S. Lee, and C. R. Choi (2010), Numerical estimates of drift loss and *Dst* effect for outer radiation belt relativistic electrons with arbitrary pitch angle, *J. Geophys. Res.*, *115*, A03208, doi:10.1029/2009JA014523.
Lakhina, G. S., B. T. Tsurutani, O. P. Verkhoglyadova, and J. S. Pickett (2010), Pitch angle transport of electrons due to cyclotron interactions with coherent chorus subelements, *J. Geophys. Res.*, *115*, A00F15, doi:10.1029/2009JA014885.
Lam, M. M., and B. A. Tinsley (2015), Solar wind-atmospheric electricity-cloud microphysics connections to weather and climate, *J. Atmos. Sol. Terr. Phys*, doi:10.1016/j.jastp.2015.10.019.
Lam, M. M., G. Chisham, and M. P. Freeman (2013), The interplanetary magnetic field influences mid-latitude surface atmospheric pressure, *Env. Res. Lett.*, *8*, doi:10.1088/1748-9326/8/4/045001.
Lew, J. S. (1961), Drift rate in a dipole field, *J. Geophys. Res.*, *66*, 2681, doi:10.1029/JZ066i009p02681.
Li, X., I. Roth, M. Temerin, J. R. Wygant, M. K. Hudson, and J. B. Blake (1993), Simulation of the prompt energization and transport of radiation belt particles during the March 24, 1991 SSC, *Geophys. Res. Lett.*, *20*, 2423, doi:10.1029/93GL02701.
Liu, K., D. Winske, S. P. Gary, and G. D. Reeves (2012), Relativistic electron scattering by large amplitude electromagnetic ion cyclotron waves: The role of phase bunching and trapping, *J. Geophys. Res.*, *117*, A06218, doi:10.1029/2011JA017476.
Meredith, N. P., R. B. Horne, and R. R. Anderson (2001), Substorm dependence of chorus amplitudes: Implications for the acceleration of electrons to relativistic energies, *J. Geophys. Res.*, *106*, 13,165, doi:10.1029/2000JA900156.
Meredith, N. P., R. B. Horne, R. H. A. Iles, R. M. Thorne, D. Heynderickx, and R. R. Anderson (2002), Outer zone relativistic electron acceleration associated with substorm-enhanced whistler mode chorus, *J. Geophys. Res.*, *107*(A7), 1144, doi:10.1029/2001JA9009700.
Meredith, N. P., M. Cain, R. B. Horne, R. M. Thorne, D. Summers, and R. R. Anderson (2003a), Evidence for chorus-driven electron acceleration to relativistic energies from a survey of geomagnetically disturbed periods, *J. Geophys. Res.*, *108*(A6), 1248, doi:10.1029/2002JA009764.
Meredith, N. P., R. M. Thorne, R. B. Horne, D. Summers, B. J. Fraser, and R. R. Anderson (2003b), Statistical analysis of relativistic electron energies for cyclotron resonance with EMIC waves observed on CRRES, *J. Geophys. Res.*, *108*(A6), 1250, doi:10.1029/2002JA009700.
Meredith, N. P., R. B. Horne, S. A. Glauert, R. M. Thorne, D. Summers, J. M. Albert, and R. R. Anderson (2006), Energetic outer zone electron loss timescales during low geomagnetic activity, *J. Geophys. Res.*, *111*, A05212, doi:10.1029/2005JA011516.
Meredith, N. P., R. B. Horne, M. M. Lam, M. H. Denton, J. E. Borovsky, and J. C. Green (2011), Energetic electron precipitation during high-speed solar wind stream driven storms, *J. Geophys. Res.*, *116*, A05223, doi:10.1029/2010JA016293.
Millan, R. M., and R. M. Thorne (2007), Review of radiation belt relativistic electron losses, *J. Atmos. Sol. Terr. Phys.*, *69*, 362, doi:10.1016/j.jastp.2006.06.019.
Miyoshi, Y., A. Morioka, T. Obara, H. Misawa, T. Nagai, and Y. Kasahara (2003), Rebuilding process of the outer radiation belt during the 3 November 1993 magnetic storm: NOAA and Exos-D observations, *J. Geophys. Res.*, *108*(A1), 1004, doi:10.1029/2001JA007542.
Miyoshi, Y., K. Sakaguchi, K. Shiokawa, D. Evans, J. Albert, M. Connors, and V. Jordanova (2008), Precipitation of radiation belt electrons by EMIC waves, observed from ground and space, *Geophys. Res. Lett.*, *35*, L23101, doi:10.1029/2008GL035727.
Miyoshi, Y., R. Kataoka, Y. Kasahara, A. Kumamoto, T. Nagai, and M. F. Thomsen (2013), High-speed solar wind with southward interplanetary magnetic field causes relativistic electron flux enhancements of the outer radiation belt via enhanced condition of whistler waves, *Geophys. Res. Lett.*, *40*, 4520–4525, doi:10.1002/grl50916.
Morley, S. K., R. H. W. Friedel, T. E. Cayton, and E. Noveroske (2010), A rapid and prolonged electron radiation belt dropout observed with the Global Positioning System constellation, *Geophys. Res. Lett.*, *37*, L06102, doi:10.1029/2010GL0427772.
Mourenas, D., A. V. Artemyev, Q. Ma, O. V. Agapitov, and W. Li (2016), Fast dropouts of multi-MeV electrons due to combined effects of EMIC and whistler mode waves, *Geophys. Res. Lett.*, *43*, 4155–4163, doi:10.1002/2016GL068921.
Ness, N. F., and J. M. Wilcox (1964), Solar origin of the interplanetary magnetic field, *Phys. Rev. Lett.*, *13*(461), 1964.
Nicolet, M. (1975), On the production of nitric oxide in the stratosphere by oxidation of nitrous oxide, *Ann. Geophys.*, *28*, 751.
O'Brien, B. J., C. D. Laughlin, J. A. Van Allen, and L. A. Frank (1962), Measurements of the intensity and spectrum of electrons at 1000-kilometer altitude and high latitudes, *J. Geophys. Res.*, *67*, 1209, doi:10.1029/JZ067i004p01209.
Oberheide, J., K. Shiokawa, S. Gurubaran, W. E. Ward, H. Fujiwara, M. J. Kosch, J. J. Makela, and H. Takahashi (2015), The geospace response to variable inputs from the lower atmosphere: A review of the progress made by Task Group 4 of CAWSES-II, *Prog. Earth Plan. Sci.*, doi:10.1186/s40645-014-0031-4.
Olson, J. V., and L. C. Lee (1983), PC1 wave generation by sudden impulses, *Plan. Spa. Sci.*, *31*, 295.
Omura, Y., and Q. Zhao (2013), Relativistic electron microbursts due to nonlinear pitch angle scattering by EMIC triggered emissions, *J. Geophys. Res. Space Physics*, *118*, 5008–5020, doi:10.1002/jgra.50477.
Omura, Y., Y. Katoh, and D. Summers (2008), Theory and simulation of the generation of whistler-mode chorus, *J. Geophys. Res.*, *113*, A04223, doi:10.1029/2007JA012622.
Omura, Y., Y. Miyashita, M. Yoshikawa, D. Summers, M. Hikishima, Y. Ebihara, and Y. Kubota (2015), Formation processes of relativistic electron flux through interaction with chorus emissions in the Earth's inner magnetosphere, *J. Geophys. Res. Space Physics*, *120*, 9545–9562, doi:10.1002/2015JA021563.
Onsager, T. G., R. Grubb, J. Kunches, L. Matheson, D. Speich, R. Zwickl, and H. Sauer (1996), Operational uses of the GOES energetic particle detectors, *SPIE*, *2812*, 281.
Onsager, T. G., G. Rostoker, H. J. Kim, G. D. Reeves, T. Obara, H. J. Singer, and C. Smith (2002), Radiation belt electron flux dropouts: Local time, radial and particle-energy dependence, *J. Geophys. Res.*, *107*(A11), 1382, doi:10.1029/2001JA000187.

Owens, M. J., C. J. Scott, A. J. Bennett, S. R. Thomas, M. Lockwood, R. G. Harrison, and M. M. Lam (2015), Lightning as a space-weather hazard: UK thunderstorm activity modulated by the passage of the heliospheric current sheet, *Geophys. Res. Lett.*, *42*, 9624–9632, doi:10.1002/2015GL066802.

Palmer, C. E. (1959), The stratospheric polar vortex in winter, *J. Geophys. Res.*, *64*, 749, doi:10.1029/JZ064i007p00749.

Park, J.-S., K.-H. Kim, K. Shiokawa, D.-H. Lee, E. Lee, H.-J. Kwon, H. Jin, and G. Jee (2016), EMIC waves observed at geosynchronous orbit under quiet geomagnetic conditions ($Kp \leq 1$), *J. Geophys. Res. Space Physics*, *121*, 1377–1390, doi:10.1002/2015JA021968.

Paulikas, G., and J. B. Blake (1979), Effects of the solar wind on magnetospheric dynamics: Energetic electron at the synchronous orbit, in *Quantitative Modeling of Magnetospheric Processes, Geophys. Monogr. Ser.*, vol. 21, edited by W. Olsen, pp. 180–202, AGU, Washington, D. C.

Pesnell, W. D., R. A. Goldberg, C. H. Jackman, D. L. Chenette, and E. E. Gaines (1999), A search of UARS data for ozone depletions caused by the highly relativistic electron precipitation events of May 1992, *J. Geophys. Res.*, *104*, 165, doi:10.1029/1998JA900030.

Pizzo, V. J. (1985), Interplanetary shocks on the large scale: A retrospective on the last decade's theoretical efforts, in *Collisionless Shocks in the Heliosphere: Reviews of Current Research*, *Geophys. Monogr. Ser.*, vol. 35, edited by B. T. Tsurutani and R. G. Stone, 51 pp., AGU, Washington, D. C.

Rae, I. J., I. R. Mann, K. R. Murphy, L. G. Ozeke, D. K. Milling, A. A. Chan, S. R. Elkington, and F. Honary (2012), Ground-based magnetometer determination of in situ Pc4-5 ULF electric field wave spectra as a function of solar wind speed, *J. Geophys. Res.*, *117*, A04221, doi:10.1029/2011JA017335.

Reed, R. J., J. L. Wolfe, and H. Nishimoto (1963), A spectral analysis of the energetics of the stratospheric sudden warming of early 1957, *J. Atmos. Sci.*, *20*, 256, doi:10.1175/1520-0469(1963)020<0256:ASAOTE>2.0.CO;2.

Reeves, G. D., et al. (2013), Electron acceleration in the heart of the Van Allen radiation belts, *Science*, *341*, 991, doi:10.1126/science.1237743.

Remya, B., B. T. Tsurutani, R. V. Reddy, G. S. Lakhina, and R. Hajra (2015), Electromagnetic cyclotron waves in the dayside subsolar outer magnetosphere generated by enhanced solar wind pressure: EMIC wave coherency, *J. Geophys. Res. Space Physics*, *120*, 7536–7551, doi:10.1002/2015JA021327.

Roederer, J. G., and H. Zhang (2014), *Dynamics of Magnetically Trapped Particles—Foundations of the Physics of Radiation Belts and Space Plasmas*, Springer, Heidelberg, New York, Dordrecht, London.

Ronnmark, K. (1982), WHAMP: Waves in homogeneous anisotropic multicomponent plasma, *Kiruna Geophys. Inst. Rep., 179*, Kiruna Geophys. Inst., Kiruna, Sweden.

Rusch, D. W., J.-C. Gerard, S. Solomon, P. J. Crutzen, and G. C. Reid (1981), The effect of particle precipitation events on the neutral and ion chemistry of the middle atmosphere—I. Odd nitrogen, *Planet Space Sci.*, *29*, 767–774, doi:10.1016/0032-0633(81)90048-9.

Sakaguchi, K., K. Shiokawa, Y. Miyoshi, Y. Otsuka, T. Ogawa, K. Asamura, and M. Conners (2008), Simultaneous appearance of isolated auroral arcs and Pc 1 geomagnetic pulsations at subauroral latitudes, *J. Geophys. Res.*, *113*, A05201, doi:10.1029/2007JA012888.

Scherhag, R. (1952), Die explosionsartige stratosphaerenerwarmung des Spaetwinters 1951/1952, *Ber. Deut. Wetterdienstes*, *6*, 51.

Scherhag, R. (1960), Stratospheric temperature changes and the associated changes in pressure distribution, *J. Meteor.*, *17*(6), 575, doi:10.1175/1520-0469(1960)017<0575:STCATA>2.0.CO;2.

Schoeberl, M. R. (1978), Stratospheric warmings: Observations and theory, *Rev. Geophys. Space Phys.*, *16*, 521, doi:10.1029/RG016i004p00521.

Schröter, J., B. Heber, F. Steinhilber, and M. B. Kallenrode (2005), Energetic particles in the atmosphere: A Monte-Carlo simulation, *Adv. Space Res.*, *37*, 1597–1601, doi:10.1016/j.asr.2005.05.085.

Sckopke, N. A. (1966), A general relation between the energy of trapped particles and the disturbance field near the Earth, *J. Geophys. Res.*, *71*, 3125, doi:10.1029/JZ071i013p03125.

Shiokawa, K., et al. (2010), The STEL induction magnetometer network for observation of high-frequency geomagnetic pulsations, *Earth Planets Space*, *62*, 517, doi:10.5047/eps.2010.05.003.

Shprits, Y., M. Daae, and B. Ni (2012), Statistical analysis of phase space density buildup and dropouts, *J. Geophys. Res.*, *117*, A01219, doi:10.1029/2011JA016939.

Shprits, Y. Y., R. M. Thorne, R. Friedel, G. D. Reeves, J. Fennell, D. N. Baker, and S. G. Kanekal (2006), Outward radial diffusion driven by losses at magnetopause, *J. Geophys. Res.*, *111*, A11214, doi:10.1029/2006JA011657.

Sinnhuber, M., H. Nieder, and N. Wieters (2012), Energetic particle precipitation and the chemistry of the mesosphere/lower thermosphere, *Surv. Geophys.*, *33*, 1281, doi:10.1007/s10712-012-9201-3.

Smith, E. J., and B. T. Tsurutani (1976), Magnetosheath lion roars, *J. Geophys. Res.*, *81*, 2261, doi:10.1029/JA081i013p02261.

Smith, E. J., and J. H. Wolfe (1976), Observations of interaction regions and corotating shocks between one and five AU: Pioneers 10 and 11, *Geophys. Res. Lett.*, *3*, 137, doi:10.1029/GL003i003p00137.

Smith, E. J., B. T. Tsurutani, and R. L. Rosenberg (1978), Observations of the interplanetary sector structure up to heliographic latitudes of 16°: Pioneer 11, *J. Geophys. Res.*, *83*, 717, doi:10.1029/JA083iA02p00717.

Sonnerup, B. U., and L. J. Cahill Jr. (1967), Magnetopause structure and attitude from Explorer 12 observations, *J. Geophys. Res.*, *72*, 171, doi:10.1029/JZ072i001p00171.

Southwood, D. J., et al. (2001), Magnetometer measurements from the Cassini Earth swingby, *J. Geophys. Res.*, *106*, 30,109, doi:10.1029/2001JA900110.

Su, Z., H. Zhu, F. Xiao, H. Zheng, C. Shen, Y. Wang, and S. Wang (2013), Latitudinal dependence of nonlinear interaction between electromagnetic ion cyclotron wave and radiation belt relativistic electrons, *J. Geophys. Res. Space Physics*, *118*, 3188–3202, doi:10.1002/jgra.50289.

Suess, S. T., and S. F. Nerney (2001), Stagnation flow in streamer boundaries, *Astrophys. J.*, *565*, 1275, doi:10.1086/324697.

Summers, D., and R. M. Thorne (2003), Relativistic electron pitch-angle scattering by electromagnetic ion cyclotron waves during geomagnetic storms, *J. Geophys. Res.*, *108*(A4), 1143, doi:10.1029/2002JA009489.

Takada, A., et al. (2011), Observation of diffuse cosmic and atmospheric gamma rays at balloon altitudes with an electron-tracking Compton camera, *Astrophys. J.*, *733*, 13, doi:10.1088/0004-637X/733/1/13.

Tanimori, T., et al. (2015), An electron-tracking Compton telescope for a survey of the deep universe by MeV gamma-rays, *Astrophys. J.*, *810*, 28, arXiv:1507.03850, doi:10.1088/0004-637X/810/1/28.

Thorne, R. M. (1977), Influence of relativistic electron precipitation of the lower ionosphere and stratosphere, in *Dynamical and Chemical Coupling*, edited by B. Grandal and J. A. Holtet, pp. 161–168, D. Reidel, Dordrecht, Netherlands.

Thorne, R. M. (1980), The importance of energetic particle precipitation on the chemical composition of the middle atmosphere, *Pageoph*. vol. 118, Birkhaeuser Verlag, Basel, Switzerland.

Thorne, R. M., and C. F. Kennel (1971), Relativistic electron pitch-angle scattering by electromagnetic ion cyclotron waves during geomagnetic storms, *J. Geophys. Res.*, *76*, 4446, doi:10.1029/JA076i019p04446.

Thorne, R. M., et al. (2013), Rapid local acceleration of relativistic radiation-belt electrons by magnetospheric chorus, *Nature Lett.*, *504*, 411, doi:10.1038/nature12889.

Tinsley, B. A., and G. W. Deen (1991), Apparent tropospheric response to MeV-GeV particle flux variations: A connection via electrofreezing of supercooled water in high-level clouds?, *J. Geophys. Res.*, *96*, 22,283, doi:10.1029/91JD02473.

Tinsley, B. A., J. T. Hoeksema, and D. N. Baker (1994), Stratospheric volcanic aerosols and changes in air-earth current density at solar wind magnetic sector boundaries as conditions for the Wilcox tropospheric vorticity effect, *J. Geophys. Res.*, *99*, 16,805, doi:10.1029/94JD01207.

Tsurutani, B. T., and W. D. Gonzalez (1987), The cause of High-Intensity, Long-Duration Continuous AE Activity (HILDCAAs): Interplanetary Alfvén wave trains, *Planet Space Sci.*, *35*, 405, doi:10.1016/0032-0633(87)90097-3.

Tsurutani, B. T., and G. S. Lakhina (1997), Some basic concepts of wave-particle interactions in collisionless plasmas, *Rev. Geophys.*, *35*, 491–502, doi:10.1029/97RG02200.

Tsurutani, B. T., and E. J. Smith (1977), Two types of magnetospheric ELF chorus and their substorm dependences, *J. Geophys. Res.*, *82*, 5112–5128, doi:10.1029/JA082i032p05112.

Tsurutani, B. T., E. J. Smith, H. I. West Jr., and R. M. Buck (1979), Chorus, energetic electrons and magnetospheric substorms, in *Wave Instabilities in Spa. Plas*, edited by P. J. Palmadesso and K. Papadopoulos, 55 pp., D. Reidel, Dordrecht, Netherlands.

Tsurutani, B. T., T. Gould, B. E. Goldstein, W. D. Gonzalez, and M. Sugiura (1990), Interplanetary Alfvén waves and auroral (substorm) activity: IMP-8, *J. Geophys. Res.*, *95*, 2241, doi:10.1029/JA095iA03p-2241.

Tsurutani, B. T., W. D. Gonzalez, A. L. C. Gonzalez, F. Tang, J. K. Arballo, and M. Okada (1995), Interplanetary origin of geomagnetic activity in the declining phase of the solar cycle, *J. Geophys. Res.*, *100*, 21,717–21,733, doi:10.1029/95JA01476.

Tsurutani, B. T., X.-Y. Zhou, V. M. Vasyliunas, G. Haerendel, J. K. Arballo, and G. S. Lakhina (2001), *Interplanetary Shocks, Magnetopause Boundary Layers and Dayside Auroras: The Importance of a Very Small Magnetospheric Region*, *Surv. Geophys.*, vol. 22, 101 pp., Kluwer Acad., Netherlands.

Tsurutani, B. T., J. K. Arballo, X.-Y. Zhou, C. Galvan, and J. K. Chao (2002), Electromagnetic electron and proton cyclotron waves in geospace: A Cassini snapshot, in *Space Weather Study Using Multipoint Techniques*, edited by L.-H. Lyu, pp. 97–125, Pergamon, Elsevier Science Ltd.

Tsurutani, B. T., W. D. Gonzalez, F. Guarneri, Y. Kamide, X. Zhou, and J. K. Arballo (2004), Are High-Intensity Long-Duration Continuous AE Activity (HILDCAA) events substorm expansion events?, *J. Atmos. Sol. Terr. Phys.*, *66*, 167, doi:10.1016/j.jastp.2003.08.015.

Tsurutani, B. T., et al. (2006), Corotating solar wind streams and recurrent geomagnetic activity: A review, *J. Geophys. Res.*, *111*, A07S01, doi:10.1029/2005JA011273.

Tsurutani, B. T., E. Echer, F. L. Guarnieri, and J. U. Kozyra (2008), CAWSES November 7–8, 2004, superstorm: Complex solar and interplanetary features in the post-solar maximum phase, *Geophys. Res. Lett.*, *35*, L06S05, doi:10.1029/2007/GL031473.

Tsurutani, B. T., O. P. Verkhoglyadova, G. S. Lakhina and S. Yagitani (2009), Properties of dayside outer zone chorus during HILDCAA events: Loss of energetic electrons, *J. Geophys. Res.*, *114*, A03207, doi:10.1029/2008JA013353.

Tsurutani, B. T., R. B. Horne, J. S. Pickett, O. Santolik, D. Schriver, and O. P. Verhoglyadova (2010), Introduction to the special section on chorus: Chorus and its role in space weather, *J. Geophys. Res.*, *115*, A00F01, doi:10.1029/2010JA015870.

Turner, D. L., et al. (2014a), On the cause and extent of outer radiation belt losses during the 30 September 2012 dropout event, *J. Geophys Res. Space Physics*, *119*, 1530–1540, doi:10.1002/2013JA019446.

Turner, D. L., et al. (2014b), Competing source and loss mechanisms due to wave-particle interactions in Earth's outer radiation belt during the 30 September to 3 October 2012 geomagnetic storm, *J. Geophys. Res. Space Physics*, *119*, 1960–1979, doi:10.1002/2014JA019770.

Usanova, M. E., I. R. Mann, J. Bortnik, L. Shao, and V. Angelopoulos (2012), THEMIS observations of electromagnetic ion cyclotron wave occurrence: Dependence on *AE*, *SYM-H*, and solar wind dynamic pressure, *J. Geophys. Res.*, *117*, A10218, doi:10.1029/2012JA018049.

Usanova, M. E., et al. (2014), Effect of EMIC waves on relativistic and ultrarelativistic electron populations: Ground-based and Van Allen Probes observations, *Geophys. Res. Lett.*, *41*, 1375–1381, doi:10.1002/2013GL059024.

Van Allen, J. A., and L. A. Frank (1959), Radiation measurements to 658,300 km with Pioneer IV, *Nature*, *184*, 219, doi:10.1038/184219a0.

Verkhoglyadova, O. P., B. T. Tsurutani, and G. S. Lakhina (2010), Properties of obliquely propagating chorus, *J. Geophys. Res.*, *115*, A00F19, doi:10.1029/2009JA014809.

Vernov, S. N., A. E. Chudakov, P. V. Vakulov, Y. I. Logachev, and A. G. Nikolayev (1960), Radiation measurements during the flight of the second Soviet space rocket, in *Space Research: Proceedings of the First International Space Science Symposium*, edited by H. Kallmann-Bijl, 845 pp., North-Holland Publ. Co., Amsterdam.

West, H. I., Jr., R. M. Buck, and J. R. Walton (1972), Shadowing of electron azimuthal-drift motions near the noon magnetopause, *Nature Phys. Sci.*, *240*, 6, doi:10.1038/physci240006a0.

Wilcox, J. M., P. H. Scherrer, L. Svalgaard, W. O. Roberts, and R. H. Olson (1973), Solar magnetic sector structure: Relation to circulation of the Earth's atmosphere, *Science*, *180*, 185, doi:10.1126/science.180.4082.185.

Winterhalter, D. E., E. J. Smith, M. E. Burton, N. Murphy, and D. J. McComas (1994), The heliospheric plasma sheet, *J. Geophys. Res.*, *99*, 6667, doi:10.1029/93JA03481.

Wissing, J. M., and M.-B. Kallenrode (2009), Atmospheric Ionization Module Osnabrück (AIMOS): A 3-D model to determine atmospheric ionization by energetic charged particles from different populations, *J. Geophys. Res.*, *114*, A06104, doi:10.1029/2008JA013884.

Zhou, X., and B. T. Tsurutani (1999), Rapid intensification and propagation of the dayside aurora: Large scale interplanetary pressure pulses (fast shocks), *Geophys. Res. Lett.*, *26*, 1097, doi:10.1029/1999GL900173.

Zhou, X.-Y., and B. T. Tsurutani (2001), Interplanetary shock triggering of nightside geomagnetic activity: Substorms, pseudobreakups, and quiescent events, *J. Geophys. Res.*, *106*, 18,957, doi:10.1029/2000JA003028.

Zhou, X.-Y., R. J. Strangeway, P. C. Anderson, D. G. Sibeck, B. T. Tsurutani, G. Haerendel, H. U. Frey, and J. K. Arballo (2003), Shock aurora: FAST and DMSP observations, *J. Geophys. Res.*, *108*(A4), 8019, doi:10.1029/2002JA009701.

Zhou, X.-Y., K. Fukui, H. C. Carlson, J. I. Moen, and R. J. Strangeway (2009), Shock aurora: Ground-based imager observations, *J. Geophys. Res.*, *114*, A12216, doi:10.1029/2009JA014186.